Cement and Concrete Research 178 (2024) 107461

Contents lists available at ScienceDirect

Cement and Concrete Research

journal homepage: www.elsevier.com/locate/cemconres

# Hydrothermal synthesis of sodium silicate from rice husk ash: Effect of synthesis on silicate structure and transport properties of alkali-activated concrete

Mohammed Fouad Alnahhal [a], Abdelrahman Hamdan [a], Ailar Hajimohammadi [a], Arnaud Castel [b], Taehwan Kim [a,*]

[a] Centre for Infrastructure Engineering and Safety, School of Civil and Environmental Engineering, University of New South Wales, Sydney, NSW 2052, Australia
[b] School of Civil and Environmental Engineering, University of Technology Sydney (UTS), Sydney, NSW 2007, Australia

ARTICLE INFO

*Keywords:*
Sodium silicate
Alkaline activator
Sustainability
Durability
Chloride resistance

ABSTRACT

Alkali-activated materials (AAMs) are increasingly being researched to reduce the reliance on conventional cements as building materials. However, expensive and energy-intensive alkaline activators curtail the usage of AAMs. Waste-derived alkaline activators are effective in mitigating the environmental concerns for alkaline activators, but their synthesis process and the transport properties of AAM concrete are yet to be fully understood. This paper presents comprehensive results of syntheses of alternative sodium silicates (SSs) from rice husk ash (RHA) using a hydrothermal process. The effect of mixing duration, temperature, and RHA/NaOH ratio on the availability and structure of silicate species in the extracted RHA SSs were investigated. Compressive strength, water absorption, sorptivity, and chloride resistance tests were carried out to assess the performance of RHA SS in AAM concrete. The results showed that all RHA SSs contain monomer, dimer, trimer, and tetramer silicate oligomers but their respective proportion primarily depends on the temperature and RHA/NaOH ratio. The recommended hydrothermal process in this study was 1 h of mixing at 80 °C. The 28-day compressive strength of AAM concrete made of RHA SS was only up to 5 % lower than the one made of commercial SS. In addition, the transport properties of AAM concrete made of RHA and commercial SSs were comparable, proving the feasibility of RHA-derived activators (filtered and unfiltered).

## 1. Introduction

In light of achieving sustainable development in the construction industry, mitigation of the carbon footprint of concrete has become indispensable. Due to the economic recovery from the global COVID-19 pandemic, the worldwide consumption of ordinary Portland cement (OPC) has increased by about 5 % in 2021 compared to 2020 reaching 4.4 billion tonnes [1]. Alkali-activated materials (AAMs) have emerged as an eco-friendly resource with great potential to reduce the dependency on OPC [2–5]. Nevertheless, there is a consensus by researchers that the widespread acceptance of AAM systems is impacted by the need for alkaline hydroxides and silicates in this technology [6]. The overall cost and embodied energy associated with these alkaline activators are considerably high, which is a challenging problem to be resolved to increase the sustainability of AAM concrete [7]. To achieve a balance between the reduction of the greenhouse gas emissions and the technological development in the construction industry, sustainable AAM concrete can be developed by maximising durability and by embracing sustainable activators [8,9]. Taking into consideration typical concrete mix proportions for AAM systems, the alkaline activator solution (i.e., alkaline silicates, hydroxides, and water) constitutes a minor portion, about 7–10 % by weight of concrete [10–13]. However, the activator is considered as the main contributor responsible for ~60 % of the total environmental impacts of AAMs [13].

While the design of AAM concrete in its beginnings was limited to conventional activators, using waste-derived activators from various silica-rich resources has been considered later on, including rice husk ash (RHA) [14,15], waste glass [16], silica fume [17], and bottom ash [18]. Previous studies showed that the synthesis of alternative sodium silicates from these resources is viable and yields an activator comparable to commercial ones [19–21]. Consequently, the global warming potential associated with AAMs made of waste-derived activators can be

* Corresponding author.
*E-mail address:* taehwan.kim@unsw.edu.au (T. Kim).

https://doi.org/10.1016/j.cemconres.2024.107461
Received 20 September 2023; Received in revised form 4 February 2024; Accepted 12 February 2024
Available online 19 February 2024

almost halved [19]. Despite the promising potential to develop waste-derived alkaline activators, the properties of activators synthesised from RHA have not been fully understood in terms of the effects of the extraction process on the structures of the silicates. In addition, the effect of extracted activators on the transport properties (e.g., water absorption and chloride penetration) of AAM concrete has not fully been studied either.

Various studies have shown promising results on silicate extraction from RHA [8,14,20]. Silicate extraction from RHA can be carried out in an alkaline medium using sodium hydroxide (NaOH). Comparable mechanical and microstructural properties were achieved for AAMs activated with RHA-derived and commercial sodium silicates. However, there is a lack of comprehensive research on the effect of the extraction process on the dissolution efficiency and the structures of silicates. Oligomerisation of silicates, which describes the formation of complex molecules from small ones, is dictated by the silica/alkali ratio [22,23]. Therefore, when dissolving RHA into alkaline solutions, the dissolved silica content is expected to significantly affect the structure and the oligomerisation level of the silicate species in the system. Although sodium silicates derived from RHA offer many advantages over the commercial ones, the effect of different parameters on the extent of availability and the oligomerisation of silicates from RHA requires further research to be successfully applied in AAMs.

First, the chemical composition and the silicate speciation of the RHA-derived activators can widely vary due to the effect of several factors relating to the extraction efficiency, especially silicate availability [8]. The availability of silicates in the activator is essential for initiating the polycondensation reaction (i.e., geopolymerisation) and the hardening of AAM [24]. The release rate of silica into the NaOH solution can be greatly affected by several parameters, including the processing duration, temperature, NaOH molarity, and amorphous silica content in RHA [14,20]. Second, the transport properties of AAM concrete with RHA-derived activators has not been fully investigated by previous studies [19–21]. The non-dissolved particles from the dissolution process of silica-rich wastes can affect the microstructure properties, especially when using unfiltered waste-derived activators [25,26]. A non–homogeneous microstructure indicates higher susceptibility towards the penetration of fluids, which in turn increases the deterioration of the concrete [27]. Therefore, the study of the effect of alternative activators is of primary importance in controlling the performance of AAMs. The results from previous studies were limited to the effect of waste-derived activators on microstructural and hardened properties [16,28,29], and knowledge gaps currently exist on the transport properties.

This study focuses on two aspects: i) to understand the effect of the hydrothermal process on both availability and structure of silicate species in solutions derived from RHA, and ii) to provide insights into the hardened and transport properties (including water absorption and chloride resistance) of AAM concrete prepared with filtered and unfiltered RHA-derived sodium silicates compared to the commercially available one. The authors' previous work [15] presented the rheological properties and structural build-up of AAM pastes made of RHA SSs from the fresh condition to the final setting. The current study is the result of the continuous endeavour to develop more sustainable AAM concrete by conducting a detailed synthesis process of RHA SSs with the aim of reducing the high embodied energy associated with commercial alkaline activators. A hydrothermal process was used by mixing RHA and NaOH solution at different processing durations (1 to 5 h of stirring), temperatures (60 to 100 °C), and the RHA/NaOH ratios. The dissolution of RHA and the availability of silicate were measured using an inductively coupled plasma-optical emission spectrometer (ICP-OES). The structure of silicate species was studied using an attenuated total reflection Fourier transform infrared (ATR-FTIR) and $^{29}Si$ nuclear magnetic resonance (NMR). Moreover, the viscosity of silicate solutions was determined using a dynamic rheometer. After that, the hardened properties and chloride resistance of AAM concrete using the optimised RHA-derived activator were examined. Three different chloride resistance tests (modified ASTM C1202 [30], NT Build 492 [31], and ASTM C1556 [32]) were carried out in this study. Those results were then compared to previous results for AAM concrete to determine the validity of the standardised tests originally developed for conventional concrete (Portland cement-based concrete).

## 2. Experimental programme

### 2.1. Materials

RHA purchased from NK Enterprises, India (product commercial name: Silpozz) was used in this study as a silica source to produce alternative sodium silicate (SS) solutions. In addition, two precursors were used to prepare AAM concrete: i) ground granulated blast furnace slag (GGBFS), and ii) Class F fly ash conforming to ASTM C618 [33]. The specific gravities of RHA, GGBFS, and fly ash were 2.2, 2.8, and 2.1, respectively. The oxide composition of RHA, GGBFS, and fly ash obtained from X-ray fluorescence (PANalytical AXIOS instrument) are shown in Table 1. The particle size distributions of three materials were determined using the laser diffraction particle size analyser (Mastersizer 2000, Malvern Panalytical, UK) and plotted in Fig. 1. The median particle size of RHA, GGBFS, and fly ash were 18 μm, 11 μm, and 22 μm, respectively. To show the particle shape and surface texture of three materials, the secondary scanning electron microscopy (SEM) images are shown in Fig. 2. As expected, fly ash is composed of spherical particles compared to the GGBFS and RHA consisting of more irregular shapes of particles.

The Rietveld XRD quantification refinement of RHA was carried out in the authors' previous study [15]. The silica in RHA was composed of 85.5 wt% amorphous phase and 14.5 wt% crystalline phases (quartz and cristobalite). Since RHA is primarily composed of silica (91.9 % obtained from the XRF analysis), the amorphous phase was assumed to be non-crystalline $SiO_2$. Therefore, 91.9 % of $SiO_2$ in the RHA can be segmented as 78.6 % amorphous and 13.3 % crystalline silica. In addition, 2 % of the loss on ignition (LOI) was obtained from RHA as the result of the unburnt carbon, which was supported by the 2.5 % mass loss from the thermogravimetric analysis in $N_2$ flux (see detailed analysis in ref. [15]).

NaOH pellets (98.0 % purity, Chem-Supply Pty Ltd. Australia) were used to prepare the solution for RHA SS synthesis and the activator for AAM concrete mixtures. The alkaline activator used in the preparation of AAM concrete was a mixture of sodium hydroxide solution (10 M NaOH) and sodium silicate solutions. Three SS solutions were used in concrete, including i) commercial SS composed of 29.4 wt% $SiO_2$, 14.7 wt% $Na_2O$, and 55.9 wt% water supplied by PQ Australia, ii) filtered RHA SS, and iii) unfiltered RHA SS.

River sand and crushed basalt aggregates were used in the preparation of AAM concretes. The maximum aggregate size was 4.75 mm and 20 mm for the sand and coarse aggregates, respectively.

**Table 1**
Chemical compositions of RHA, GGBFS, and fly ash.

| Oxide compositions (%) | RHA | GGBFS | Fly ash |
|---|---|---|---|
| $SiO_2$ | 91.86 | 31.52 | 66.56 |
| $Al_2O_3$ | 0.61 | 12.22 | 22.47 |
| CaO | 1.03 | 44.53 | 1.64 |
| MgO | 0.67 | 4.62 | 0.65 |
| $Fe_2O_3$ | 0.58 | 1.14 | 3.54 |
| $K_2O$ | 1.91 | 0.33 | 1.75 |
| $Na_2O$ | 0.14 | 0.21 | 0.58 |
| $SO_3$ | 0.06 | 3.24 | 0.10 |
| LOI | 2.00 | 0.79 | 1.66 |

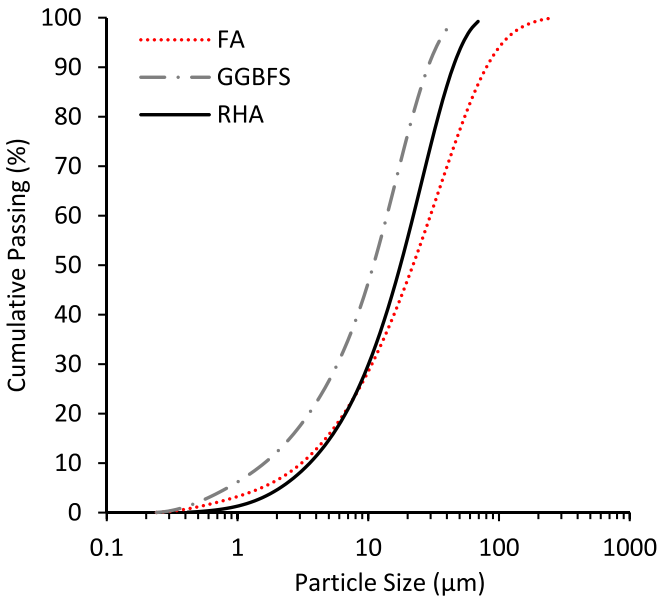


**Fig. 1.** The particle size distributions of FA, GGBFS and RHA.

### 2.2. Sodium silicate synthesis from RHA

SS solutions were synthesised from RHA using a hydrothermal process (heating and stirring), as shown in Fig. 3. This process was commonly used by previous researchers to produce alternative SS solutions [8,18,34,35]. In this study, several suspensions were produced using combinations of RHA, NaOH, and water. The suspensions were exposed to heating and stirring to induce the dissolution of silica from RHA into the NaOH solution.

Dissolution of silica from RHA is influenced by many factors, such as reaction duration and temperature. Therefore, three sets of parameters shown in Table 2 were chosen for analysis. *Set I* for the effect of heating duration, *Set II* for the effect of heating temperature, and *Set III* for the effect of $SiO_2/Na_2O$ weight ratios obtained by mixing an increased amount of RHA in the NaOH solution. It is worth mentioning that in *Set I* and *Set II*, the proportions of RHA, NaOH and water were chosen to make the theoretical $SiO_2/Na_2O$ weight ratio of 2.0, which is equivalent to the ratio found in the commercial SS used. As mentioned in Section 2.1, 78.6 % of amorphous $SiO_2$ seems to be more appropriate to compute the $SiO_2/Na_2O$ ratio because the total content of $SiO_2$ includes not only the reactive silica phase (mostly amorphous) but also low (or non) reactive phases. However, Set I and Set II of synthesis designs used the total content of $SiO_2$ (91.9 wt%) obtained from XRF (see Table 1) to compute the ratio of $SiO_2/Na_2O$, as shown in Table 2. This is because i) using the total $SiO_2$ was much simpler to compute the $SiO_2/Na_2O$ ratio since the Rietveld analysis of X-ray diffraction spectrum is not always a viable option in practice and ii) either using the amorphous silica content or using the total content of silica content would not practically affect the optimisation of the parameters in this study.

The preparation process started by mixing NaOH pellets and water. After allowing the NaOH solution to cool down to the room temperature, RHA was added and mixed at different temperatures and durations using a temperature-controlled hot plate. Glass microfibre filters (Grade GF/C with 1.2 μm pore size) were then used to remove the undissolved residues and to determine the dissolution efficiency. The filtered solutions were then analysed. The filtration setup is illustrated in Fig. 4. To remove the SS entrapped in the residues after the filtration, the solid residues were washed with isopropanol, and then placed in the oven to eliminate the free water. After that, the dried residues were weighed to determine the dissolution efficiency by considering the weight difference between RHA used and residues. Unfiltered RHA SS solution was also prepared separately using the optimised stirring time and temperature to study the effect of the residues on the strength and chloride

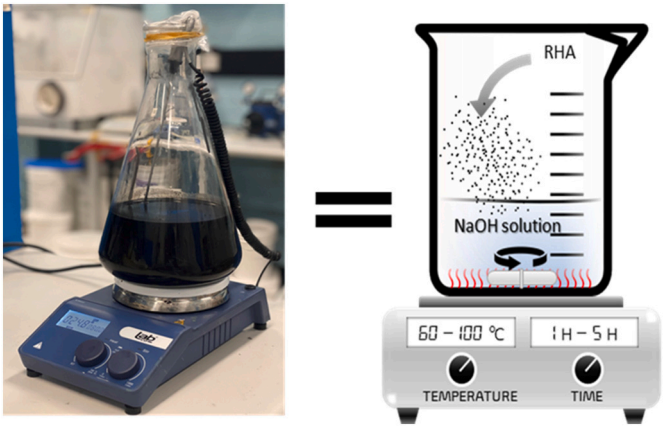


**Fig. 3.** The hydrothermal process used for the extraction of silica from RHA [8].

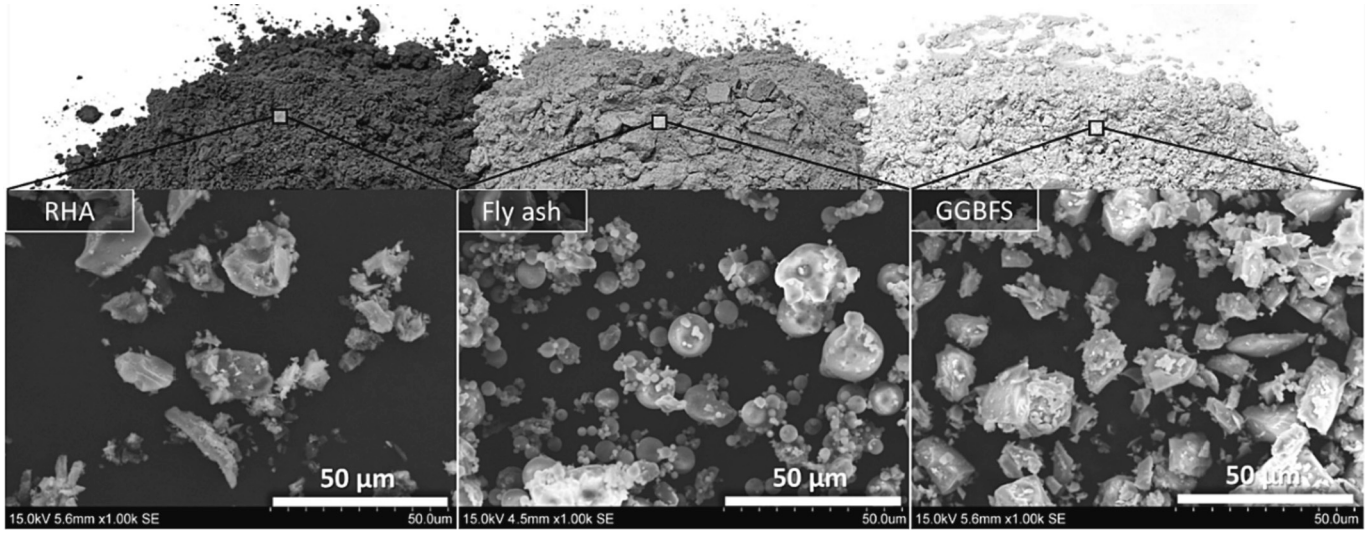


**Fig. 2.** Photos and secondary SEM images of RHA, fly ash and GGBFS.

**Table 2**
Different parameters used in the development of the RHA SSs.

| Mixtures | | Duration, h | Temp., °C | $SiO_2/Na_2O$ weight ratio | $SiO_2/Na_2O$ molar ratio | RHA, g[a] | NaOH pellets, g[b] | Water, g |
|---|---|---|---|---|---|---|---|---|
| | D1 | 1 | 80 | 2.00 | 2.07 | 218 (200) | 129 (100) | 352 |
| | D2 | 2 | 80 | 2.00 | 2.07 | 218 (200) | 129 (100) | 352 |
| Set I | D3 | 3 | 80 | 2.00 | 2.07 | 218 (200) | 129 (100) | 352 |
| | D4 | 4 | 80 | 2.00 | 2.07 | 218 (200) | 129 (100) | 352 |
| | D5 | 5 | 80 | 2.00 | 2.07 | 218 (200) | 129 (100) | 352 |
| | T60 | 1 | 60 | 2.00 | 2.07 | 218 (200) | 129 (100) | 352 |
| | T70 | 1 | 70 | 2.00 | 2.07 | 218 (200) | 129 (100) | 352 |
| Set II | T80 | 1 | 80 | 2.00 | 2.07 | 218 (200) | 129 (100) | 352 |
| | T90 | 1 | 90 | 2.00 | 2.07 | 218 (200) | 129 (100) | 352 |
| | T100 | 1 | 100 | 2.00 | 2.07 | 218 (200) | 129 (100) | 352 |
| | R2.00 | 1 | 80 | 2.00 | 2.07 | 218 (200) | 129 (100) | 352 |
| | R2.25 | 1 | 80 | 2.25 | 2.33 | 244 (225) | 129 (100) | 352 |
| Set III | R2.50 | 1 | 80 | 2.50 | 2.58 | 272 (250) | 129 (100) | 352 |
| | R2.75 | 1 | 80 | 2.75 | 2.84 | 300 (275) | 129 (100) | 352 |
| | R3.00 | 1 | 80 | 3.00 | 3.10 | 327 (300) | 129 (100) | 352 |

[a] The value in () represents the $SiO_2$ in the RHA (91.9 % from XRF).
[b] The value in () represents the $Na_2O$ in NaOH (77.5 %).

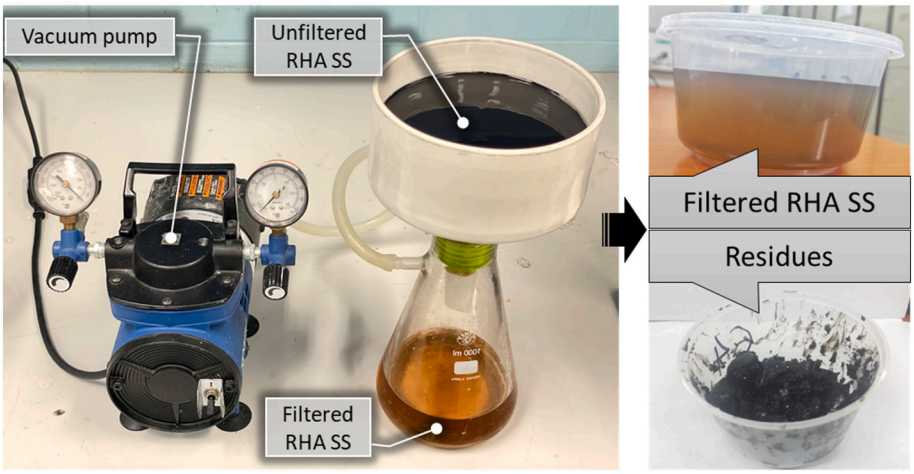


**Fig. 4.** Filtration process of RHA-derived sodium silicate.

transport properties.

### 2.3. Test methods to characterise RHA sodium silicates

#### 2.3.1. ICP-OES for chemical compositions

Si and Na concentrations were measured in the filtered solutions using ICP-OES at the Mark Wainwright Analytical Centre, UNSW Sydney. Deionised water was used to dilute the solutions as the conventional 5 % nitric acid dilution leads to polymer-like silica gel deposition [36].

#### 2.3.2. ATR-FTIR for silicate structure

The mid-infrared spectra were recorded in the range of 1300 to 700 $cm^{-1}$ wavenumbers using a diamond/ZnSe ATR crystal (3 mm diameter) with a spectral resolution of 4 $cm^{-1}$. This test facilitates understanding the structure of silicates in the RHA-derived solutions by measuring the bond vibrations between atoms. The test was carried out on the filtered solutions.

#### 2.3.3. $^{29}Si$ NMR for silicate structure

The $^{29}Si$ NMR spectra of solutions were acquired using 300 MHz Bruker Avance III spectrometer equipped with a BBFO probe. Nearly 0.6 ml of filtered solution was charged into a 5 mm NMR tube. Each spectrum was collected using 128 scans with a nearly 5-s recycle delay. The NMR spectra were processed using Bruker TOPSPIN 3.6.5 software. Deuterium oxide ($D_2O$, 99.9 %) was used as a reference to measure the signal background of silicon in the NMR tube and the probe.

#### 2.3.4. Flow sweep test for Newtonian viscosity

Discovery Hybrid Rheometer (DHR-2) with a sandblasted concentric cylinder geometry from TA Instruments was used to determine the Newtonian viscosity of the filtered RHA SS solutions. The gap width between the cup cylinder the bob cylinder was 1.16 mm. All measurements were made at 25 °C. A linear flow sweep test was performed using shear rates between 0.1 $s^{-1}$ and 100 $s^{-1}$, and the stress response at each shear rate was measured. The Newtonian viscosity was calculated from the slope of the straight-line of the points fitted in the shear stress vs. shear rate.

### 2.4. AAM concrete preparation

#### 2.4.1. Mix design

AAM concretes were prepared to study the effect of RHA SS on compressive strength, water absorption, sorptivity, and chloride resistance. To produce AAM concrete, the RHA SSs were produced using the efficient and effective hydrothermal method (one hour of mixing at 80 °C) based on the dissolution efficiency results (will be discussed in Section 3.1.1) and compressive strength of the pastes prepared using RHA SSs (presented in the Supplementary Material). The details of the results of paste samples and the selection of the most effective synthesis parameters can be found in the Supplementary Materials. Table 3 shows three different groups of concrete prepared with different $SiO_2/Na_2O$ weight ratios in the activators, namely 1.0, 1.3 and 1.6. As can be seen from Table 3, the amount of non-dissolved residues increased when the

**Table 3**
Mix proportions of AAM concretes.

| Mix | Set I | | | Set II | | | Set III | | |
|---|---|---|---|---|---|---|---|---|---|
| | C-Ms1.0-CSS | C-Ms1.0-FRSS | C-Ms1.0-UFRSS | C-Ms1.3-CSS | C-Ms1.3-FRSS | C-Ms1.3-UFRSS | C-Ms1.6-CSS | C-Ms1.6-FRSS | C-Ms1.6-UFRSS |
| FA (kg/m$^3$) | 300 | 300 | 300 | 300 | 300 | 300 | 300 | 300 | 300 |
| GGBFS (kg/m$^3$) | 100 | 100 | 100 | 100 | 100 | 100 | 100 | 100 | 100 |
| RHA residues (kg/m$^3$) | – | – | 9 | – | – | 12 | – | – | 15 |
| NaOH 10 M (kg/m$^3$) | 63 | 48 | 48 | 44 | 24 | 24 | 25 | 0 | 0 |
| Commercial SS (kg/m$^3$) | 100 | – | – | 132 | – | – | 163 | – | – |
| RHA SS (kg/m$^3$) | | | | | | | | | |
| - Filtered | – | 115 | – | – | 151 | – | – | 188 | – |
| - Unfiltered | – | – | 124 | – | – | 163 | – | – | 203 |
| Add. water (kg/m$^3$) | 78 | 78 | 78 | 71 | 71 | 71 | 65 | 65 | 65 |
| Sand (kg/m$^3$) | 777 | 777 | 768 | 777 | 777 | 765 | 777 | 777 | 762 |
| Coarse aggregate (kg/m$^3$) | 927 | 927 | 927 | 927 | 927 | 927 | 927 | 927 | 927 |
| Paste volume fraction (m$^3$/m$^3$) | 0.37 | 0.37 | 0.37 | 0.37 | 0.37 | 0.37 | 0.37 | 0.37 | 0.37 |
| w/b (wt.) | 0.44 | 0.44 | 0.44 | 0.44 | 0.44 | 0.44 | 0.44 | 0.44 | 0.44 |
| $SiO_2$ (kg/m$^3$) | 30 | 30 | 30 | 39 | 39 | 39 | 48 | 48 | 48 |
| $Na_2O$ (kg/m$^3$) | 30 | 30 | 30 | 30 | 30 | 30 | 30 | 30 | 30 |
| $SiO_2/Na_2O$ (wt.) | 1.0 | 1.0 | 1.0 | 1.3 | 1.3 | 1.3 | 1.6 | 1.6 | 1.6 |
| $Na_2O$/binder (wt%) | 7.5 % | 7.5 % | 7.5 % | 7.5 % | 7.5 % | 7.5 % | 7.5 % | 7.5 % | 7.5 % |

Notes: In the mix designation:
- C: concrete
- Ms.: $SiO_2/Na_2O$ weight ratio in the activator
- The numbers following "Ms" denotes the $SiO_2/Na_2O$ ratio in the activator
- CSS: commercial SS
- FRSS: filtered RHA SS
- UFRSS: unfiltered RHA SS
- Saturated surface dry (SSD) sand was used. Water absorption = 3.5 %
- Saturated surface dry (SSD) coarse aggregates were used. Water absorption = 1.0 %

$SiO_2/Na_2O$ weight ratio in the activator increased from 1.0 to 1.6, which allowed for investigating the effect of the RHA residues on transport properties. As discussed by Alnahhal, et al. [15], the characterisation of the residues showed that the main phase is crystalline silica (quartz and cristobalite). Therefore, the residues were considered as part of the fine aggregates. The $Na_2O$/(FA + GGBFS) was kept constant at 7.5 %. The total binder content was fixed at 400 kg/m$^3$. GGBFS content was fixed at 25 wt% of binder (20 vol% of binder) to provide suitable flowability and setting time. The concrete was designed to achieve a compressive strength of 40–45 MPa at 28 days based on trial mixes. The slump value was in the range of 195–255 mm in all mixes.

#### 2.4.2. Mixing procedure

A round pan concrete mixer was used in accordance with ASTM C192 [37]. After oven-drying the aggregates, water equivalent to the respective absorption capacity of all fine and coarse aggregates was added and mixed for 5 min prior to concrete casting. After that, FA and GGBFS were added and dry mixed for 5 min to achieve uniform dispersion. The activator (commercial or RHA SS) was then added to the dry materials and mixed for 3 min followed by a 3-min rest. A 2-min final mixing was then applied. The concrete was placed in the moulds in two layers and vibrated until the surface of the concrete became relatively smooth and the large air bubbles ceased to break through the top surface.

### 2.5. Test methods for AAM concrete

#### 2.5.1. Compressive strength

For AAM concrete, standard cylinders with 100 mm in diameter and 200 mm in height were used according to ASTM C39 [38]. All specimens were cured at room temperature (23 ± 2 °C) and sealed with a plastic sheet to prevent any moisture loss until the moment of testing (1, 7, 28, and 91 days). At each specified age, the average value of three tested specimens was considered.

#### 2.5.2. Water absorption

At the age of 28 days, 100-mm in diameter and 50-mm thick discs were sawn from concrete cylinders for the water absorption test, in accordance with ASTM C642 [39]. The oven-dry mass was first determined by placing the specimens in an oven at a temperature of 110 ± 5 °C for 24 h. After removing the specimens from the oven, they were allowed to cool in dry air to a temperature of 20 to 25 °C and the dry mass was recorded. The specimens were then immersed in water for 30 min and 72 h to determine the initial and final water absorption, respectively.

#### 2.5.3. Rate of absorption (sorptivity) of water

The sorptivity of concrete specimens was determined by measuring the increase in water depth caused by capillary suction. This can be calculated by measuring the mass change in the concrete specimen when only one surface of 100 mm diameter is exposed to water while the other surfaces are sealed. The test was carried out at the age of 28 days on concrete discs measuring 100 mm in diameter × 50 mm in height. Before starting the test, all specimens were placed in an environmental chamber at a temperature of 50 °C and relative humidity of 80 % for 3 days. After that, the specimens were placed in a sealable container and stored at 23 °C for 15 days to achieve equilibration of the moisture distribution within the test specimens in accordance with ASTM C1585 [40]. The specimens were then removed from the storage container. The side surface and the top surface of the specimen that will not be exposed to water were then sealed. Bilinear water absorption was considered to determine initial sorptivity and secondary sorptivity.

#### 2.5.4. Chloride-ion penetration

The rapid chloride penetration test (RCPT) method was carried out to assess the resistance of AAM concrete against the penetration of chloride ions in accordance with ASTM C1202 [30]. The amount of electrical current passed through 50-mm thick slices of 100-mm nominal diameter cylinders was monitored during a 6-h period using PROOVEit software from Germann Instruments. Two specimens were tested for each mix after 6 months of casting. Initially, 60 V was applied to the specimens in trial tests to get some insights about the initial current and temperature. The specimens experienced overheating and the total charge passed

exceeded 8000C after ~4 h. Thus, the test was terminated indicating the unsuitability of 60 *V* in measuring the total charge over a period of 6 h. In fact, the misleading conclusion may indicate that the concrete is rated as having very high chloride ion penetrability. However, the high initial current could be attributed to the high ionic electrical conductivity of AAM concrete due to the presence of free $Na^+$ ions in the pore solution [41,42]. Therefore, the voltage was lowered to 10 *V*, which is deemed to be suitable for AAM concrete containing <50 % GGBFS content [43]. It should be noted that the results from this test on AAM concrete may not be directly correlated to the chloride ion penetrability classifications mentioned in ASTM C1202 [30] which are designed for Portland cement concrete due to the modification applied in this study. However, this test method still can be used for evaluation purposes to make a comparative assessment between different AAM mixes. In the RCPT test, a qualitative assessment of the chloride ion penetration can be obtained in this study since the $Na_2O$ concentration was fixed in all mixes (see Table 3), and hence, the free $Na^+$ ions are expected to be similar in all mixes. Additionally, the chloride diffusion test was carried out (as explained in Section 2.5.6), which is believed to provide a quantitative assessment of chloride diffusion resistance of AAM concrete.

#### 2.5.5. Chloride migration

The non-steady-state migration (NSSM) coefficient in AAM concrete was determined in accordance with NT Build 492 [31], which is measured through the movement of chloride ions under the action of an external electrical field. Concrete specimens with a diameter of 100 mm and a thickness of 50 mm were used in the test after 6 months of casting. Two specimens were tested for each mix. An external electrical potential was applied to the specimen, which forces the chloride ions to migrate from the catholyte solution of 10 % NaCl into the specimen. The other side of the specimen was exposed to an anolyte solution of 0.3 N NaOH. The test set-up can be found in NT Build 492 [31]. The voltage was preset at 30 *V*, and the initial current was recorded to determine the test duration based on NT Build 492 [31]. The appropriate voltage and test duration for all specimens according to the initial current were 25 V and 24 h, respectively. After 24 h of test duration, the specimen was axially split, and a 0.1 M silver nitrate solution was sprayed onto the freshly split sections. The chloride penetration depth was then measured from the visible white silver chloride precipitation, after which the chloride migration coefficient was calculated from this penetration depth. The NSSM coefficient was calculated using Eq. (1).

$$D_{nssm} = \frac{0.0239(273+T)L}{(U-2)/t}\left(x_d - 0.0238\sqrt{\frac{(273+T)L\,x_d}{U-2}}\right) \quad (1)$$

where $D_{nssm}$: non-steady-state migration coefficient ($\times 10^{-12}$ $m^2/s$), *U*: absolute value of the applied voltage (*V*), *T*: average value of the initial and final temperatures in the anolyte solution (°C), *L*: thickness of the specimen (mm), $x_d$: average value of the penetration depths (mm), and *t*: test duration (h). It should be noted that the chloride concentration at which the colour changes was assumed at $c_d \approx 0.07$ N based on Portland cement-based concretes and a broader database is required to calculate $c_d$ for AAM concretes.

#### 2.5.6. Chloride diffusion

The apparent chloride diffusion coefficient ($D_a$) for AAM concrete was determined by bulk diffusion in accordance with ASTM C1556 [32]. The test measures the movement of chloride ions under a concentration gradient, from a high concentration zone to a low concentration zone. After 28 days from casting, 100-mm Ø × 75-mm thick specimens were sawn from the top of concrete cylinders. Two specimens were used for each mix. The specimens were fully sealed except the surface with 100 mm in diameter. These specimens were exposed to sodium chloride (NaCl) solution (165 g NaCl per L of solution). The specimens were removed from the NaCl solution after 35 days of exposure and a profile grinding was carried out to obtain powder samples from different depths. The powder was collected at 1 mm increments in the first 10 mm and 2 mm increments from 10 mm to 20 mm. The total (acid-soluble) chloride content of the powder samples was determined at each depth according to ASTM C1152 [44] using Metrohm 855 Robotic Titrosampler. The apparent chloride diffusion coefficient ($D_a$) was calculated by fitting the measured chloride contents at different depths using a non-linear regression analysis using the method of least squares, as shown in Eq. (2).

$$C(x,t) = C_s - (C_s - C_i)erf\left(\frac{x}{4\sqrt{D_a t}}\right) \quad (2)$$

where $C(x,t)$: chloride concentration measured at depth $x$ and exposure time $t$ (wt%), $C_s$: projected chloride concentration at the interface between the exposure liquid and test specimen that is determined by the regression analysis (wt%), $C_i$: initial chloride-ion concentration prior to submersion in the NaCl solution (wt%), $x$: depth below the exposed surface (m), $D_a$: apparent chloride diffusion coefficient ($m^2/s$), $t$: the exposure time (s), and *erf*: the error function = $erf(z) = 2/\sqrt{\pi}\int_0^z exp(-u^2)du$.

## 3. Results and discussion

### 3.1. Characterisation of RHA-derived sodium silicates

#### 3.1.1. Dissolution efficiency

Fig. 5 presents the results relating to the effect of the treatment processes on the dissolution efficiency. As it can be seen in Fig. 5, increasing the mixing duration had a minimal impact on the dissolution efficiency. The dissolved RHA slightly increased from 76 % to 83 % when the mixing duration was increased from 1 h to 5 h (*Set I*). On the other hand, increasing the mixing temperature from 60 °C to 80 °C (*Set II*) significantly increased the amount of dissolved RHA from 46 % to 76 %, but the increase in dissolution at higher temperatures was insignificant. Increasing the amount of RHA (*Set III*) resulted in more dissolved silica into the NaOH solution. However, the percentage of dissolved RHA continuously decreased from 76 % to 67 % when increasing the RHA content in the hydrothermal process. The dissolution of silica strongly depends on the temperature due to the increased dissolution rates at high temperatures [45,46]. Indeed, numerous studies revealed that various factors affect the silica dissolution kinetics into the alkali hydroxide solutions, including the particle size and surface area, amount of the amorphous phase, type and concentration of alkali metals, saturation degree with regards to the dissolving component, and reaction temperature [46–48]. In this study, the high amorphous content in the raw RHA used (78.6 %) and the high alkalinity of the NaOH solution contributed to achieving high dissolution rates of up to 83 %. Based on the dissolution efficiency of RHA, the yield of silica was optimum using 1 h of mixing at 80 °C.

The amounts of dissolved elements in the filtered solutions were analysed using ICP-OES. The elemental concentrations were then converted to the oxide weight percentage. Fig. 6 illustrates the weight percentages of $SiO_2$ and $Na_2O$ found in the RHA-derived solutions compared to the commercial one. Although the RHA, NaOH and water were designed to achieve the theoretical $SiO_2/Na_2O$ (wt%) ratio of 2.00 in *Set I* and *Set II*, the results showed that the actual ratio after the dissolution was in the range of 1.56–1.74, which was attributed to the incomplete dissolution of RHA. Therefore, in *Set III*, the amount of RHA was increased (see Table 2) to obtain similar amounts of dissolved oxides as in the commercial sodium silicate. This was achieved in the mix R3.00, where the $SiO_2/Na_2O$ ratio reached 1.97. However, the mix R3.00 was not efficient as the percentage of non-dissolved RHA was higher than in the other mixtures (see Fig. 5).

#### 3.1.2. Silicate species structure using ATR-FTIR

The extent of oligomerisation of silicate species in the activator is

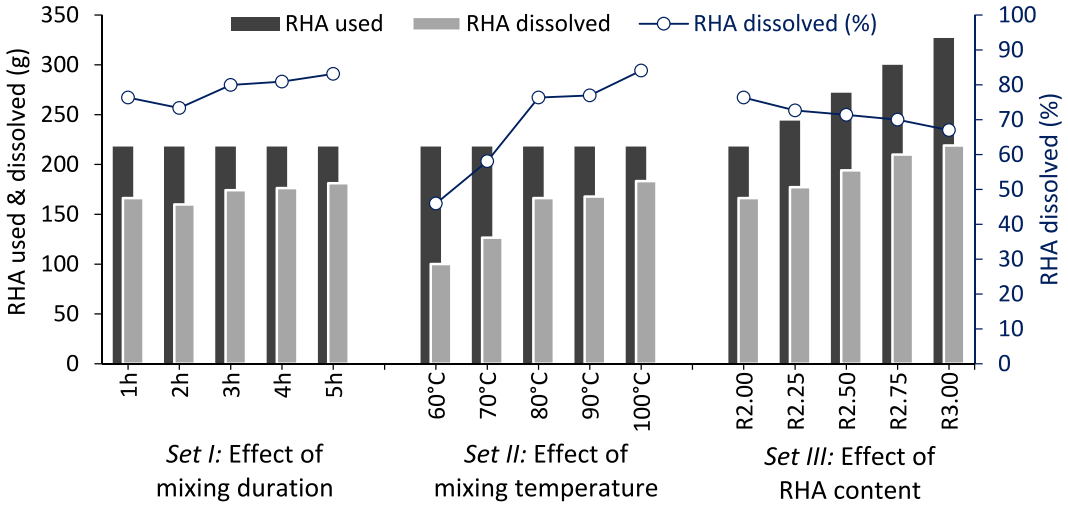


**Fig. 5.** Effect of mixing duration, temperature, and RHA content on the dissolution efficiency of RHA in NaOH solution.

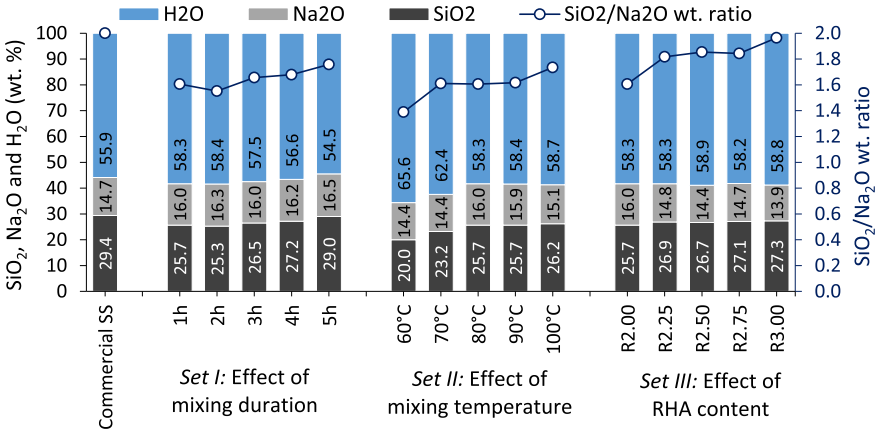


**Fig. 6.** $Na_2O$, $SiO_2$ and $H_2O$ concentrations of RHA-derived sodium silicates obtained from ICP-OES test.

primarily dictated by the availability of dissolved silicates [23,49]. To further understand the structure of the silicate network, the change in the silicate FTIR band position was used to determine the dominant silicate species in the solution [22]. Silicates with different structures have infrared bands at different frequencies within 800 $cm^{-1}$ to 1300 $cm^{-1}$ wavenumbers [49–52].

As discussed in Section 3.1.1 (see Fig. 6), the $SiO_2/Na_2O$ ratio of the RHA-derived sodium silicates varied between 1.39 and 1.97, depending on the treatment process. As a result, the silicate structure in each mix is expected to be different from the others. Fig. 7 presents the FTIR spectra of all solutions. Generally, three bands of superimposed peaks of silicates were observed at around 855, 980 and 1120 $cm^{-1}$ wavenumbers. The absorption peak at 855 $cm^{-1}$ is most likely due to monomer vibrations and some contribution from dimers [53]. The most dominant peak is centred at about 980 $cm^{-1}$, which is a contribution from monomer, dimer, trimer and tetramer anion types [22]. The shoulder at around 1120 $cm^{-1}$ is assigned to much more complex structures (e.g., cubic and caged-like structures) [23,54] along with a small contribution of colloidal silicate [55], and more siliceous solutions have more intense shoulders at this range [22,53]. It can be seen from Fig. 7 that the shoulder at ~1120 $cm^{-1}$ is more prominent in the RHA SS with higher $SiO_2/Na_2O$ ratios. This reflects the oligomerisation of silicates into complex oligomers at higher ratios [51,55].

In *Set I*, when the mixing duration was increased from 1 h to 5 h, the location of the band at 980 $cm^{-1}$ was shifted to slightly higher wavenumbers (see Fig. 7a). A similar trend was also observed upon increasing the mixing temperature and the amount of RHA in *Set II* and *Set III* as shown in Fig. 7b and c, respectively. The shift of the peak 980 $cm^{-1}$ to higher wavenumbers could be attributed to the increase in the $SiO_2/Na_2O$ ratio [22]. In *Set I*, the increase in mixing duration resulted in an increase in the $SiO_2/Na_2O$ ratio from 1.61 to 1.76, which in turn shifted the wavenumber from 980 $cm^{-1}$ to 983 $cm^{-1}$. Increasing the RHA content showed a similar trend but with a higher magnitude, where the wavenumber was shifted from 980 $cm^{-1}$ to 987 $cm^{-1}$ due to the increase in the $SiO_2/Na_2O$ ratio from 1.61 to 1.97.

It is worth mentioning that the commercial SS and the mix R3.00 showed identical intensity and position in all the bands, indicating that the silicate structure and the $SiO_2/Na_2O$ ratio in R3.00 are similar to the commercial solution. However, R3.00 required mixing high amounts of RHA, resulting in lower dissolution efficiency.

### 3.1.3. *Silicate structure measured by $^{29}Si$ NMR*

Fig. 8 shows the $^{29}Si$ NMR spectra of the 10 samples, in addition to the commercial SS solution and the deuterium oxide spectra. The $Q^i_{(kR)}$ notation [22,56] was adopted here to indicate the local configuration of the silicon atoms, where $i$ is the linkage type and $k$ is the number of silicon atoms in the ring (R) structure. The features illustrated in the spectra of the SS solutions were reported previously [22,55–59]. The peaks shown in the figure are assigned to different Si—O linkage as follows: at ~ − 70.6 ppm to $Q^0$ (monomer), ~ − 78.5 ppm to $Q^1$ (dimer, linear trimer, monosubstituted cyclic trimer, and linear tetramer) ~ −80.7 ppm to $Q^2_{(3R)}$ (cyclic trimer and monosubstituted cyclic trimer), ~

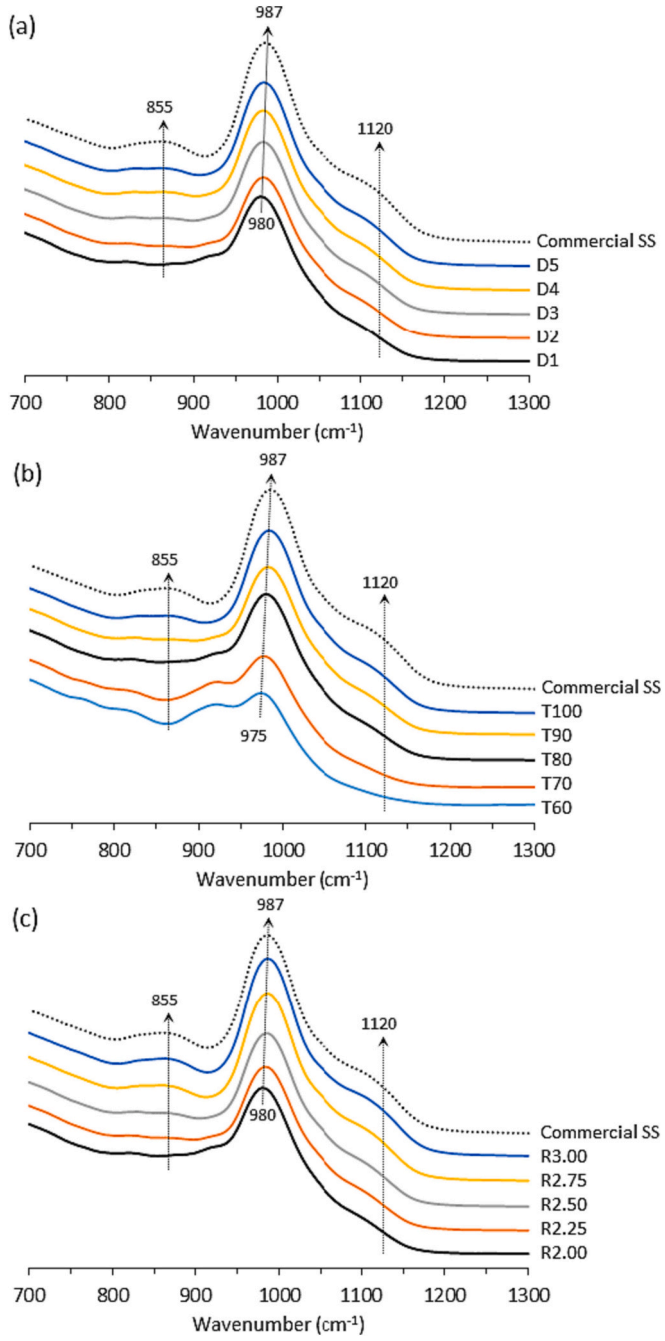


**Fig. 7.** FTIR spectra of commercial and RHA-derived sodium silicates. (a) Effect of mixing duration, (b) effect of mixing temperature, and (c) effect of RHA content.

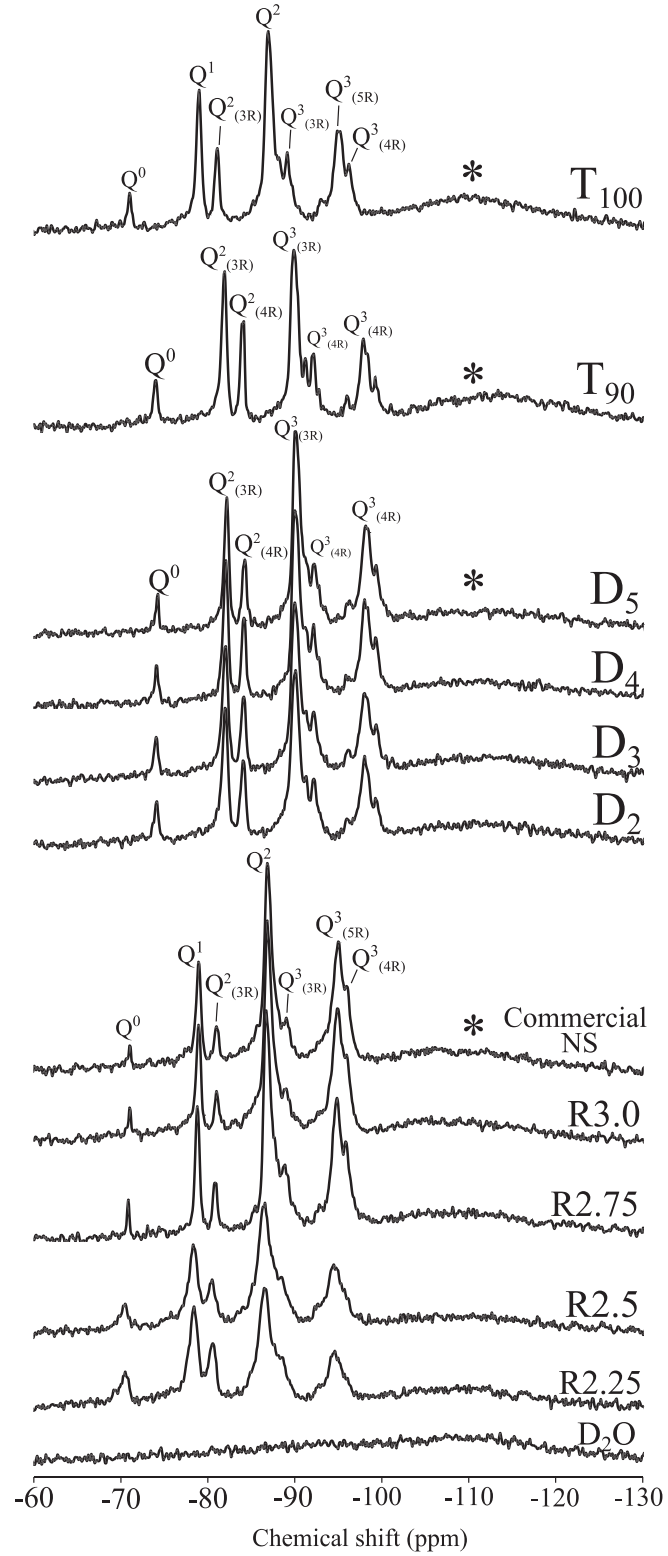


**Fig. 8.** $^{29}$Si NMR of deuterium oxide ($D_2O$) and SS solutions. The $Q^i_{(kR)}$ notation [22,56] was adopted here to indicate the local configuration of the silicon atoms, where *i* is the linkage type and *k* is the number of silicon atoms in the ring (R) structure. Asterisks denote the $Q^4$ silicate species caused by the NMR tube.

− 84.2 ppm to $Q^2_{(4R)}$ (bridged cyclic tetramers and doubly bridged cyclic tetramers), ~ − 86.6 ppm to $Q^2$ (linear trimer, linear tetramer), ~ − 89 ppm to $Q^3_{(3R)}$ (monosubstituted cyclic trimer, tricyclic hexamer and prismatic hexamer), ~ − 92.2 ppm to $Q^3_{(4R)}$ (doubly bridged cyclic tetramers), ~ − 94.7 ppm to $Q^3_{(5R)}$ (prismatic decamer) and ~ −96 ppm to $Q^3_{(4R)}$ (cubic octamer), based on results of past studies [22,55,58]. The broad low intensity peak shown at chemical shift centred at ~ − 108.7 ppm is related $Q^4$ silicate species caused by NMR tube. This is evident as the NMR spectrum of the $D_2O$ (silicon-free) solution showed such broad peak centred at ~108 ppm. Therefore, there is no colloidal silica present in the commercial and waste-derived SS solutions.

As the R (i.e., $SiO_2/Na_2O$) ratio increased in the samples, the area and intensity of the $Q^2$ and $Q^3$ signal silicate species increased while a

decrease in the intensity $Q^0$ and $Q^1$ silicate species was noticed. The $^{29}Si$ NMR spectrum of the R2.75 and R3.00 solutions were very similar to the target commercial SS solution. Moreover, the $Q^2_{(3R)}$ and $Q^3_{(3R)}$ small sharp peaks were present in the three samples and not in the low R values samples. The results regarding the effect of the R ratio are consistent with observations and conclusions of past studies which showed a consistent decrease in the $Q^0$, $Q^1$ and $Q^2$ silicate speciation on the expense of the increase in the $Q^3$ caused by the increase in the R ratio [55,59,60]. It is obvious that the stirring time had negligible effect on the silicate condensation as demonstrated by the nearly identical $^{29}Si$ NMR spectra of the $D_2$, $D_3$, $D_4$, $D_5$ samples. Increasing the temperature from 90 °C to 100 °C has considerable effect on the distribution of the Si—O linkage in the silicate anions of the solutions. Although the two $^{29}Si$ NMR spectra of the $T_{90}$ and $T_{100}$ samples exhibited similar features, it can be seen that there was a shift in the location of the peaks as the temperature increased from 90 °C to 100 °C. This may indicate a decrease in the polymerisation of the silicate species caused by a higher temperature. Kinrade and Swaddle [61] showed that silicate polymerisation was favoured at low temperatures. The $T_{100}$ SS is similar to the commercial SS one as shown in Fig. 8. However, it can be noticed that the intensities of the of the $Q^2$ and $Q^3$ silicate species in the latter are higher compared to the former. On the other hand, the intensities of the less polymerised silicate species $Q_0$ and $Q_1$ are slightly higher in the $T_{100}$ solution compared to the commercial one.

### 3.1.4. Newtonian viscosity

Fig. 9 shows the flow sweep measurements performed to determine the effect of dissolved silicates on the Newtonian viscosity of the filtered RHA SSs. The viscosity of unfiltered RHA SSs was not determined because separating the effect of dissolved silicates and undissolved particles simultaneously in the unfiltered solution would have been challenging. Therefore, the test was performed on filtered RHA SS solutions to facilitate the understanding of the effect of the silicate structure and availability on the Newtonian viscosity. Fig. 10 shows the viscosity determined as the slope of the Newtonian straight line fitted on the shear rate-stress points.

The results show that increasing the mixing duration from 1 h to 5 h leads to an increase in the viscosity from 0.070 Pa.s to 0.122 Pa.s. In terms of the effect of the mixing temperature, a drastic increase from 0.026 Pa.s to 0.126 (~5 times higher) was recorded in the viscosity when the mixing temperature was increased from 60 °C to 100 °C. A similar trend was also observed when the RHA content increased, where the viscosity of the solution R3.00 (0.173 Pa.s) was 2.5 times higher than that of R2.00 (0.070). The effect of these parameters (i.e., mixing duration, temperature, and RHA content) on the viscosity could be attributed to two factors: i) the increased concentration of silicates and ii) the change in the structure of the dissolved silicates. When comparing the results of mixing temperature (T90 and T100), an increase in the concentration of silicates was observed (see Fig. 6) but slightly less intensity of the formation of larger oligomer (see T100 and T90 in Fig. 7) was captured by $^{29}Si$ NMR. This indicates that the concentration of the silicates mainly contributes to the increase in the viscosity rather than the oligomerised silicates. However, it should be noted that the increase in the silicates concentration resulted in increasing oligomerisation at the same temperature (shown in Figs. 7 and 8). Similarly, in *Set I*, the oligomerisation of silicate species contributed to increasing the viscosity of the solutions made at longer mixing durations.

## 3.2. Performance of AAM concrete incorporated with RHA-derived activators

### 3.2.1. Compressive strength

The compressive strength of AAM concrete made of commercial SS, filtered RHA SS and unfiltered RHA SS is shown in Fig. 11. Overall, the compressive strength results showed that the effect of the type of SS used is only marginal, as the values were comparable in all mixtures. This is

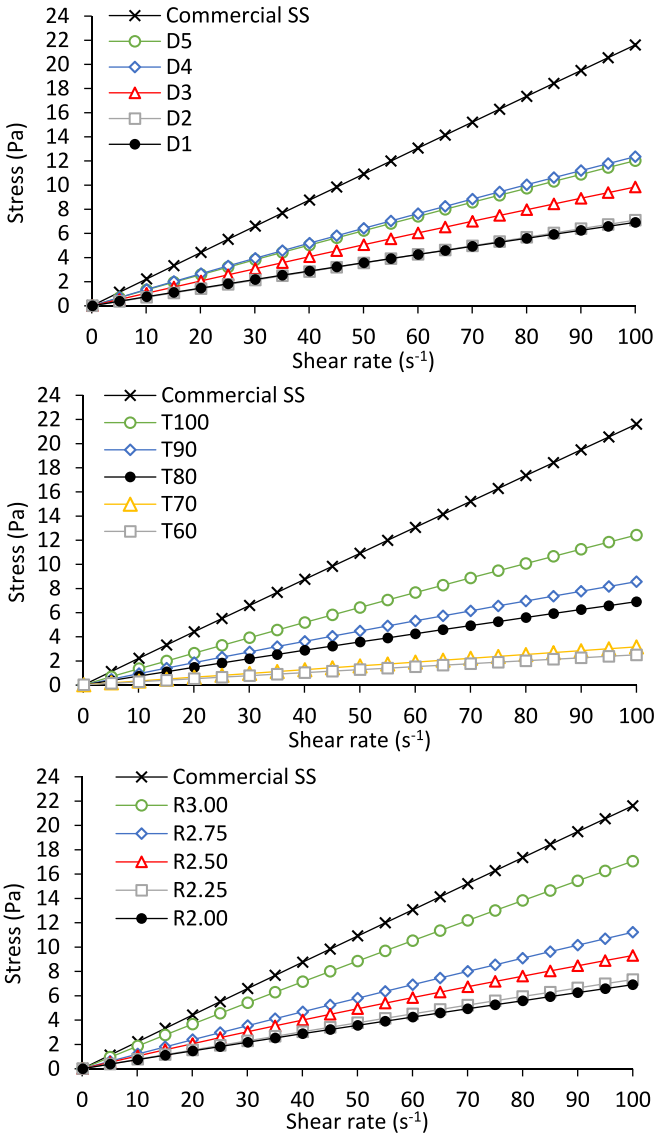


**Fig. 9.** Flow sweep test of commercial and RHA SSs.

attributed to the similar mix design parameters of the concretes from each group (see Table 3). For example, although commercial SS contains higher silicate concentrations compared to the RHA SSs, the final activator was designed to have the same $SiO_2/Na_2O$ ratio in each group by adjusting the amounts of NaOH, RHA SS and water contents. It is worth noting that the average compressive strength of the group activated with $SiO_2/Na_2O = 1.6$ was about 7 % higher than that activated with $SiO_2/Na_2O = 1.0$. This is attributed to the higher availability of silicates in the activators made of higher $SiO_2/Na_2O$ ratios. Another interesting feature of the results is the negligible effect of the unburnt carbon found in the unfiltered RHA SS on compressive strength development. A previous study by the authors [15] revealed that the unburnt carbon in the residues was about 9 % which is much higher than the 2 % observed in the raw RHA. This increase was simply the result of the relative compositional increase of carbon caused by the decrease of silica (due to dissolution) in RHA during the hydrothermal process. It was pointed out that the presence of excessive amounts of unburnt carbon in the system may result in a reduction in compressive strength [19]. In this study, a maximum amount of unburnt carbon of ~1.8 wt% (from fly ash, GGBFS and residues) was recorded for mix C-Ms1.6-UFRSS. This value is still far from the maximum LOI limit of 6 % recommended in ASTM C618 [33] for supplementary cementitious materials.

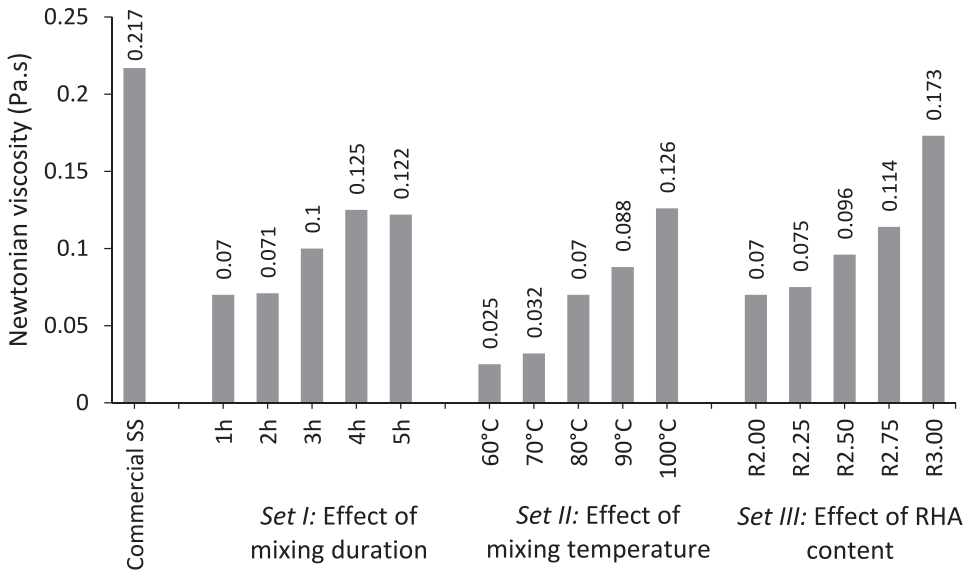


**Fig. 10.** Newtonian viscosity of commercial and RHA SSs.

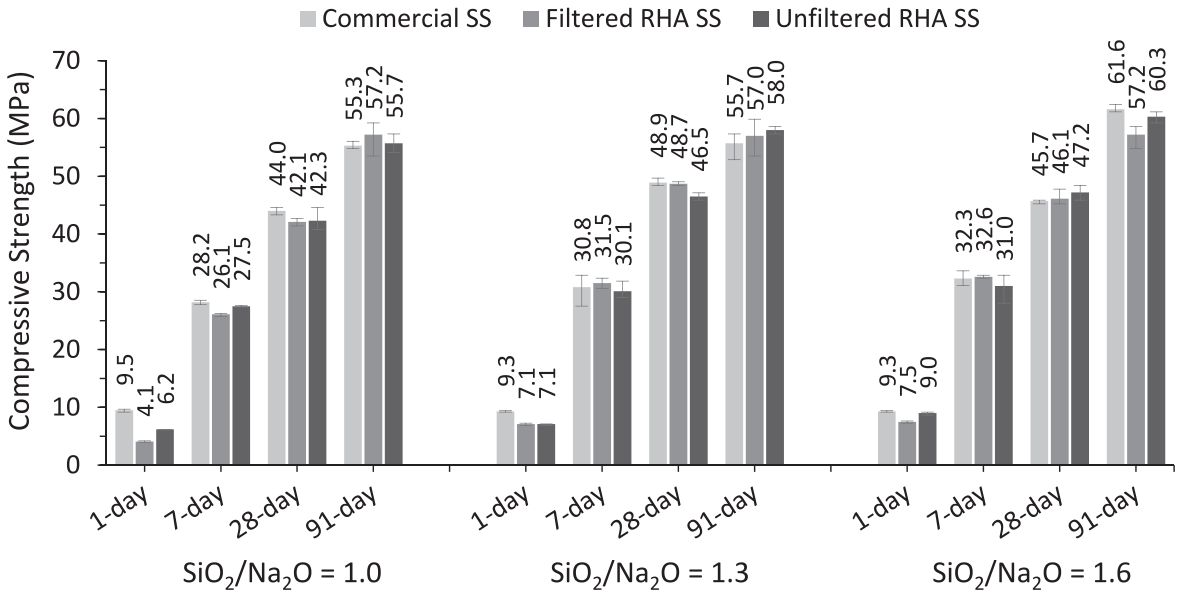


**Fig. 11.** Compressive strength of AAM concretes made of commercial and RHA-derived SSs.

### 3.2.2. *Water absorption*

Water absorption plays an important role in controlling the durability of hardened concrete and its susceptibility towards the penetration of fluids. Fig. 12 shows the water absorption percentage after immersing the concrete specimens in water for 30 min and 72 h. Overall, about 76 %–89 % of total water absorption (based on 72 h of immersion) was absorbed within 30 min and a slight further increase occurred from 30 min to 72 h of immersion. The results show that AAM concrete made of higher Ms. values absorbed more water than the concrete with lower Ms. values. For example, the initial water absorption (at 30 min) of AAM concrete made of Ms. = 1.6 was 20 %–28 % higher than that of mixes made of Ms. = 1.0. On the other hand, the final water absorption (at 72 h) of concretes made of Ms. = 1.6 was only 9 %–14 % higher than that of mixes made of Ms. = 1.0. It is well-known that the absorption of water at the initial stage is dictated by larger sizes of pores and the presence of microcracks, while smaller pores control the absorption at the later stages [62,63]. Therefore, the results of this study indicate the presence of higher macropores/microcracks in the formed microstructure of concrete made of high silica modulus (Ms) at 28 days. It is worth noting that the presence of soluble silicates in calcium-incorporated AAM systems (which is the case of this study) contributes to the reduction of the total porosity and the average pore size of the microstructure, which is attributed to the formation of pore-filling C–A–S–H gels [64]. However, the excessive availability of soluble silicates with the presence of low GGBFS contents (<25 %) leads to the formation of more aluminosilicate gel that has a more porous structure [65]. Moreover, a previous study reported the formation of microcracks at higher Ms. ratios due to the tensions caused by excessive shrinkage [63]. For sodium silicate-activated systems, Aydın and Baradan [63] observed fewer macropores and microcracks for mortars activated with Ms. = 0.8 compared to those activated with Ms. = 0.4 and Ms. = 1.2. They found that the use of a high silica modulus (i.e., Ms. = 1.2) leads to the formation of microcracks in the matrix, which in turn increases the absorption percentage of water. These results agree with those obtained in this study.

The results in Fig. 12 show that the initial and final water absorptions of concrete activated with filtered RHA SSs were similar to those

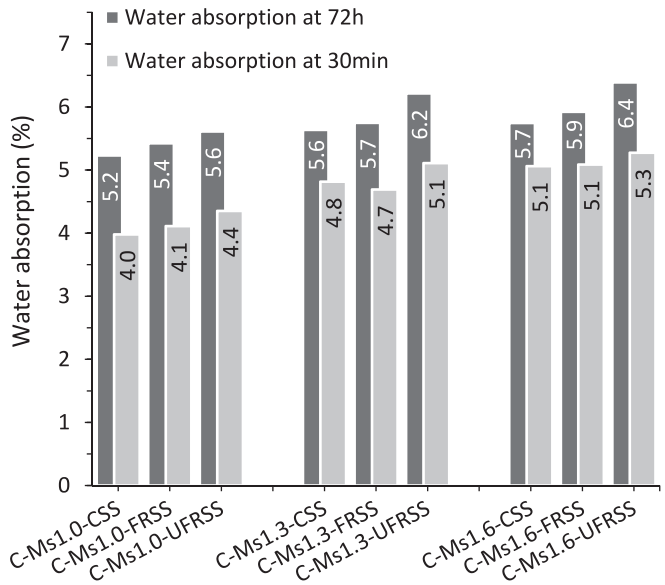


**Fig. 12.** The percentage of absorption of AAM concrete after 30 min and 72 h of immersion in water.

activated with commercial SS. On the other hand, the use of unfiltered RHA SS led to a slight increase, especially in the final water absorption. The characterisation of the undissolved residues (see Alnahhal, et al. [15]) showed that these residues were composed of 9 % of unburnt carbon. The presence of unburnt carbon in the system increases its water absorption capacity [66,67]. Zeyad, et al. [68] pointed out that the unburned carbon in binders has a negative effect on water absorption and porosity because of the shape of the cellular particle containing high porosity. Thus, the higher content of unburnt carbon in the concrete using unfiltered RHA SS seems to slightly increase the water absorption of concrete compared to that of the concrete activated with the filtered one. In addition, at a higher Ms. of 1.6, a higher amount of unfiltered RHA SS was needed (see Table 3), which in turn increased the amount of unburnt carbon and the overall water absorption.

### 3.2.3. *Rate of absorption (sorptivity) of water*

Fig. 13 presents the rate of water ingress due to capillary suction during 8 days for the AAM concrete activated with different silica moduli ratios and RHA SSs. As can be seen, the sorptivity curves show two stages. The capillary rise showed a sharp linear increase in the first stage between 0 $s^{0.5}$ and 147 $s^{0.5}$ (i.e., 0–6 h). A lower sorptivity was observed in the second stage between 1 day and 8 days. This can be explained by the fact that larger micropores/microcracks facilitate higher rates of capillary suction in the first stage and smaller pores (gel pores) control the rate of absorption at later times [62,69]. Fig. 14 presents the sorptivity values determined from Fig. 13 by calculating the slope of the line that is the best fit to the points in the range 0–6 h and 1–8 days for the initial and secondary sorptivity, respectively.

As can be observed from the results, at Ms. = 1.0, the initial sorptivity was 5–6 times higher than the secondary one. On the other hand, when Ms. increased to 1.6, the initial sorptivity was 18–23 times higher than the secondary one. In other words, increasing the Ms. value increased the initial sorptivity but led to a reduction in the secondary sorptivity. As explained in Section 3.2.2, the increase in the initial sorptivity and the decrease in the secondary one for the concretes that contain higher silicates could be attributed to the fact that the matrix has more large pores and less amount of small pores [63,70]. This was evident in the concrete with Ms. = 1.6, where the capillary suction was high at the initial stage, while the ingress of water was reduced in the secondary stage. A similar trend was observed by Borges, et al. [71] on blended metakaolin/GGBFS alkali-activated mortars.

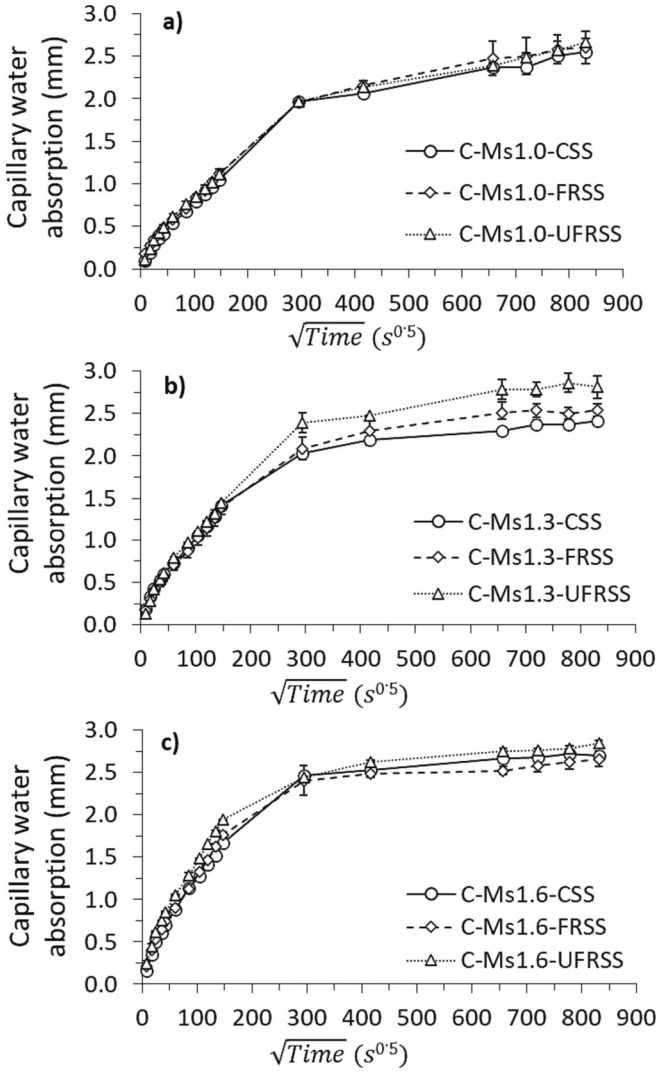


**Fig. 13.** The rate of absorption of water for AAM concrete. a) Ms. = 1.0, b) Ms. = 1.3, and c) Ms. = 1.6.

Overall, the total capillary absorption depth at the end of the sorptivity test for the specimens activated with filtered RHA SS was 2.54–2.65 mm, depending on the Ms. ratio, which is in the same range as the specimens activated with commercial SS (2.41–2.70 mm). On the other hand, a slightly higher range of 2.67–2.85 mm was recorded for the specimens activated with unfiltered RHA SS. The sorptivity results obtained from the concrete activated with commercial SS also were practically similar to those from the concrete activated with filtered RHA SS at all Ms. ratios. This indicates a similar capillary pore network within the two concrete systems. On the other hand, the initial sorptivity of specimens containing unfiltered RHA SS was slightly higher than those containing commercial and filtered RHA SSs, especially at higher Ms. ratios. For example, the initial sorptivity values for the mixes activated with unfiltered RHA SS at Ms. ratios of 1.0, 1.3 and 1.6 were 0.0067, 0.0088 and 0.0115, respectively, which is about 3 %, 7 % and 10 % higher than the corresponding initial sorptivity values obtained from the mixes activated with either filtered RHA or commercial SSs. The slight increase in sorptivity of the specimens containing unfiltered RHA SS indicates an increase in the water absorption tendency due to the presence of unburnt carbon in the residues of the unfiltered RHA SS [66,67]. A previous study on mortars containing RHA with different percentages of unburnt carbon revealed that the total capillary absorption can be significantly increased when using RHA with high amounts

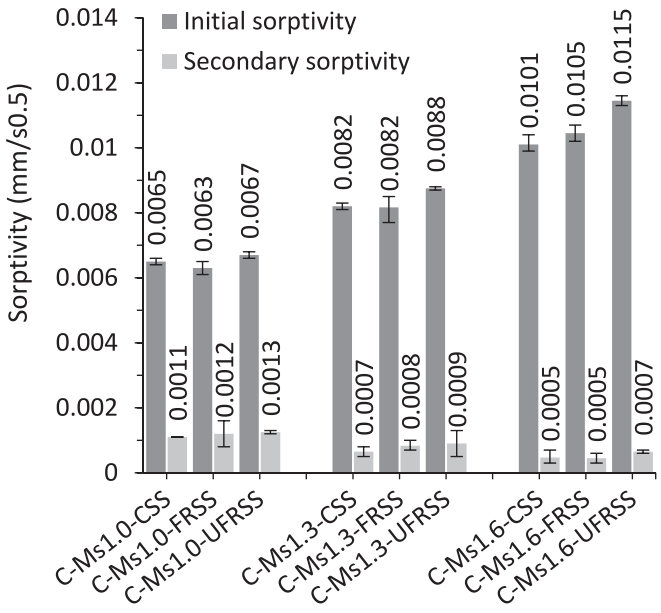


**Fig. 14.** Initial and secondary sorptivity of AAM concrete.

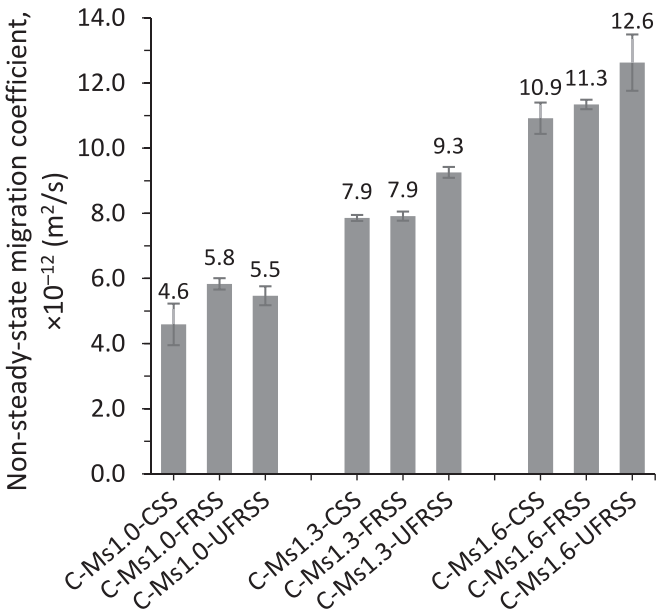


**Fig. 16.** Non-steady-state migration coefficient of AAM concrete.

of unburnt carbon [69].

### 3.2.4. Chloride resistance

*3.2.4.1. Results and analysis of accelerated chloride penetration parameters.* Figs. 15 and 16 present the modified RCPT and NSSM coefficients, respectively, for concrete specimens activated with RHA SSs with Ms. between 1.0 and 1.6 and compared to reference specimens activated with commercial SS. The modified RCPT results show that the total charge passed was within in a narrow range of 310–332, 418–449 and 528–590 coulombs for Ms. of 1.0, 1.3 and 1.6, respectively. Moreover, the NSSM coefficients followed the same trend with values in the range of 4.6–5.8 $\times 10^{-12}$ $m^2/s$, 7.9–9.3 $\times 10^{-12}$ $m^2/s$, and 10.9–12.6 $\times 10^{-12}$ $m^2/s$ for AAM concrete activated with Ms. of 1.0, 1.3 and 1.6, respectively. It can be inferred that the type of SS (i.e., commercial and RHA SSs) had an insignificant impact on the penetration of chloride ions, while a higher Ms. ratio increased both the total charge passed and the migration coefficients. The same trend was also observed in the chloride penetration depths from the migration test, as illustrated in Fig. 17.

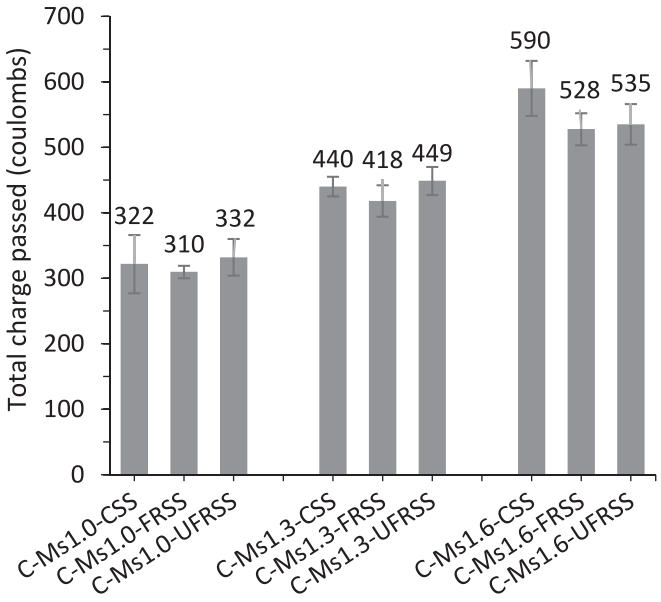


**Fig. 15.** Total charge passed through AAM concrete specimens over 6 h using 10 *V*.

*3.2.4.2. Results and analysis of chloride diffusion.* Table 4 shows the initial chloride contents ($C_i$) that were measured for all concretes prior to submersion in the exposure solution. The initial chloride contents from all concrete samples were negligibly small. Fig. 18 shows the total chloride contents (mass % of concrete) measured at each depth up to 20 mm for all AAM concretes prepared in this study. All specimens showed very low chloride contents (<0.2 % of concrete mass) at the depth of 20 mm from the surface, which implies the suitability of the maximum depth used in this study. The apparent chloride diffusion coefficient ($D_a$) was then calculated and summarised in Fig. 19. The $D_a$ values were in the range of 14.3–24.8 $\times 10^{-12}$ $m^2/s$, 25.1–35.5 $\times 10^{-12}$ $m^2/s$ and 33.4–42.8 $\times 10^{-12}$ $m^2/s$ for concretes activated with Ms. of 1.0, 1.3 and 1.6, respectively. Similar to the RCPT and NSSM results reported previously, the $D_a$ values showed a general increasing trend when the Ms. ratio increased in the activating solution. The chloride profiles recorded in this study were similar to those obtained by Babaee and Castel [65] for AAM concrete of similar composition (25 % GGBFS and 75 % fly ash). Moreover, the same trend was observed by Babaee and Castel [65] for the effect of Ms. ratio, where the $D_a$ value increased from 14 $\times 10^{-12}$ $m^2/s$ to 55 $\times 10^{-12}$ $m^2/s$ when Ms. was increased from 1.0 to 1.5.

*3.2.4.3. Discussion on chloride resistance.* A rapid indication of AAM concrete resistance to the penetration of chloride ions was evaluated using two accelerated methods, namely modified RCPT and NSSM. In modified RCPR, a slight modification was made due to the high electrical conductivity of AAM concrete by lowering the voltage to 10 *V* instead of 60 V mentioned in the standard test method described in ASTM C1202 [30]. On the other hand, the standard NSSM test is deemed to be more reliable as a rapid indication of AAM concrete resistance to the penetration of chloride ions since the test voltage and duration can be adjusted based on the initial current [31]. Because the modified RCPT and NSSM have not been fully validated for rapidly evaluating the chloride resistance of AAM systems, the bulk diffusion test was also carried out as a more reliable method to determine the resistance of concrete against the transport of chloride ions. The immersion of concrete specimens in 16.5 % NaCl solution allows for determining the chloride diffusion coefficient that reflects the chloride penetration of

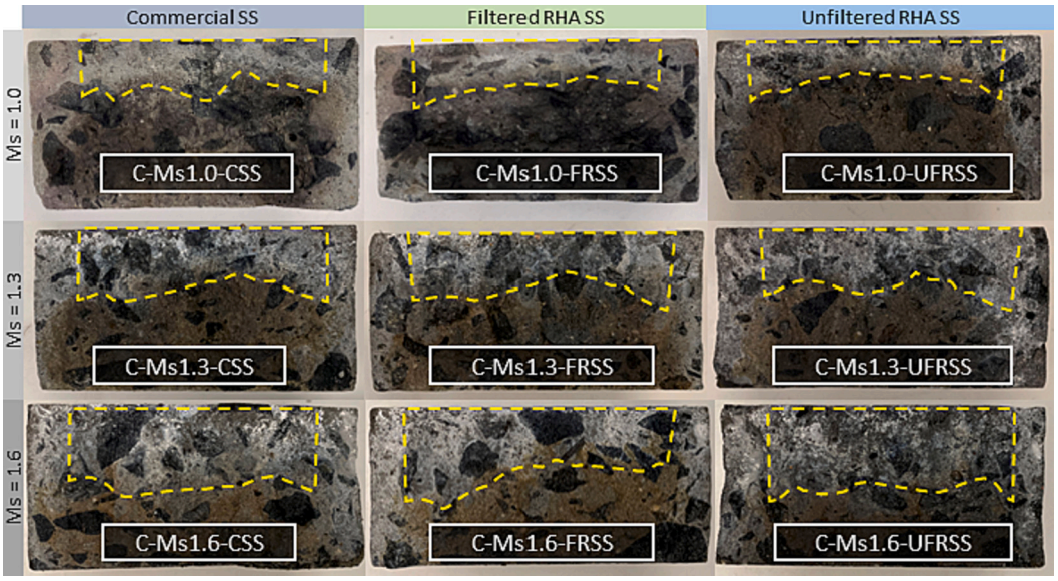


**Fig. 17.** Illustration of chloride penetration depths from the migration test. The average of 5 different depths was taken from the highlighted area.

**Table 4**
Mass % of the initial chloride content ($C_i$) of the concrete prior to submersion in the exposure solution.

| Mix | $C_i$ (mass %) |
|---|---|
| C-Ms1.0-CSS | 0.0065 |
| C-Ms1.0-FRSS | 0.0214 |
| C-Ms1.0-UF RSS | 0.0151 |
| C-Ms1.3-CSS | 0.0157 |
| C-Ms1.3-FRSS | 0.0176 |
| C-Ms1.3-UFRSS | 0.0185 |
| C-Ms1.6-CSS | 0.0126 |
| C-Ms1.6-FRSS | 0.0337 |
| C-Ms1.6- UFRSS | 0.0177 |

concrete. First, a correlation with the total charge passed was made to validate the modified RCPT results. Fig. 20 shows the correlation between the diffusion coefficient and total charge passed at 10 *V* obtained from this study. In addition, the results of comparable AAM concrete (i.e., GGBFS <25 % and similar activator) by Noushini [72] were also added to the analysis. As can be seen from Fig. 20, the total charge passed at 10 V showed a good correlation with the diffusion coefficient. It should be noted that the total charge passed at 60 V was also investigated and was substantially high (>8000 coulombs) as explained in Section 2.5.4. This confirms that the high charge passed at 60 V is not indicative of a very high chloride-ion penetrability in AAM concrete. Instead, the high charge passed at 60 V could be attributed to the presence of huge amounts of free $Na^+$ ions in the pore solution, which have been previously reported to have a significant impact on the total charge passed [41,42]. In low-calcium AAM systems, it is well-known that a higher dose of $Na_2O$ is usually needed to activate the precursor and achieve sufficient strength [11,73], which in turn increases the availability of free $Na^+$ ions. Therefore, the total charge passed at 60 V would be considerably high in these systems compared to low-calcium AAMs and cement-based concrete. The free $Na^+$ ions in the pore solution are more or less identical in all mixes used in this study due to the fixed amount of $Na_2O$ (see Table 3). Thus, the variation in the charge passed could be related to the matrix connectivity, and the chloride penetrability can be compared between the different mixes.

The correlation between chloride diffusion and migration coefficients is presented in Fig. 21. The diffusion coefficient from the total chloride content profile was generally higher than the migration coefficients. Similar behaviour was also reported by Noushini [72] on comparable mixes. As mentioned in Section 2.5.5, the chloride concentration at the colour change boundary used to calculate the chloride migration coefficients was based on Portland cement based concrete due to lack of data related to AAM concrete. Therefore, the pore solution pH of AAM concrete may affect the chloride concentration at the colour change boundary of the silver nitrate colorimetric measurement ($c_d$), leading to lower values of migration coefficients [74].

The three different chloride resistance tests carried out using the different mixtures of alkali-activated concrete revealed an insignificant effect of the type of SS compared to the effect of the Ms. value (see Figs. 15, 16, and 19). Higher Ms. ratios generally resulted in higher susceptibility to chloride penetration in the concrete. The adverse effect of increasing the silicate content on the transport of chloride-ion has been explained in literature for two reasons. One could be that the high availability of silicates from the activating solution is not favoured along with the presence of low contents of GGBFS (<25 %), leading to the formation of more aluminosilicate gel that has a porous structure compared to the pore-filling C–A–S–H gel [65]. This is in good agreement with Lee and Lee [75] who reported higher chloride penetration depths for AAMs with higher amounts of aluminosilicate gel. It is worth mentioning that, in GGBFS-dominated systems (>50 % GGBFS), the adverse effect of higher silicates on the chloride diffusion can be diminished due to the dominance of pore-filling C–A–S–H gel in favour of porous aluminosilicate gel [64,65]. Another reason could be attributed to the higher interconnectivity in the microstructure when higher Ms. ratios are used. It is well documented that the excessive use of silicate in the activating solution (i.e. very high $SiO_2/Na_2O$ ratios) results in larger shrinkage, and consequently, increases the possibility of microcracks propagation [76,77]. This leads to the passage of more chloride ions. The overall effect of Ms. was evident in the mixes activated with higher ratios, recording higher charge passed from the modified RCPT (see Fig. 15), higher chloride penetration depths from the migration test (see Fig. 17), and higher chloride diffusion coefficients (see Fig. 19). Although the concrete activated with unfiltered RHA SS had slightly higher water absorption than those activated with commercial and filtered RHA SSs (see Sections 3.2.2 and 3.2.3), the results show that the influence of Ms. on chloride-ion penetration would exceed the influence of undissolved particles found in the unfiltered RHA SS.

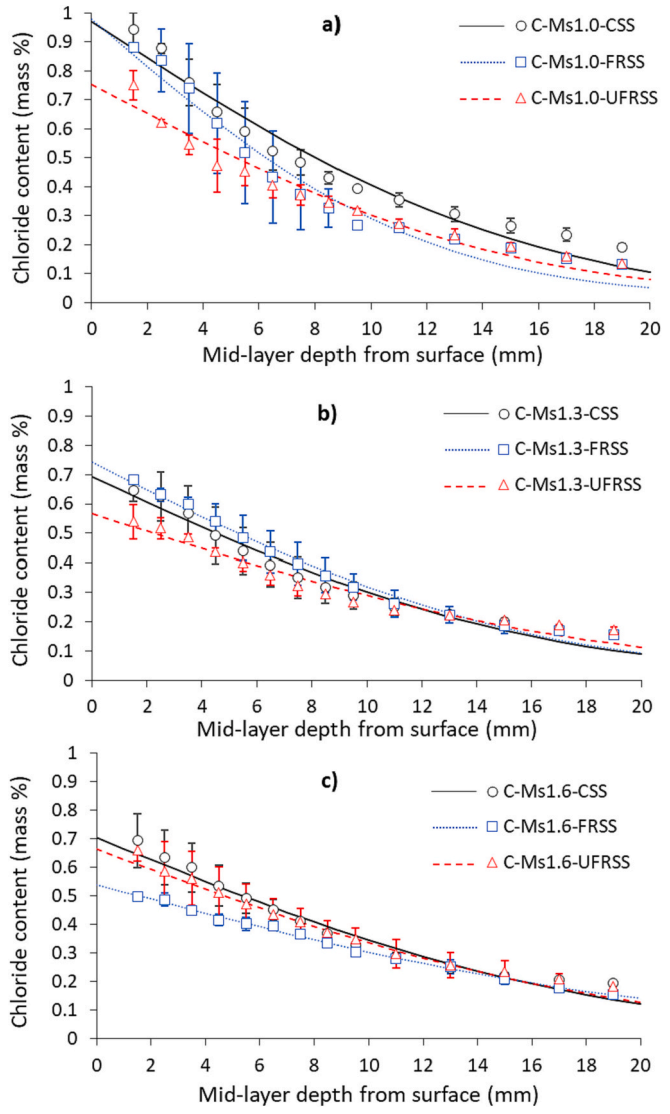


**Fig. 18.** Total chloride profiles and non-linear regression analysis measured using bulk diffusion test after 35 days of exposure. a) Ms. = 1.0, b) Ms. = 1.3, and c) Ms. = 1.6.

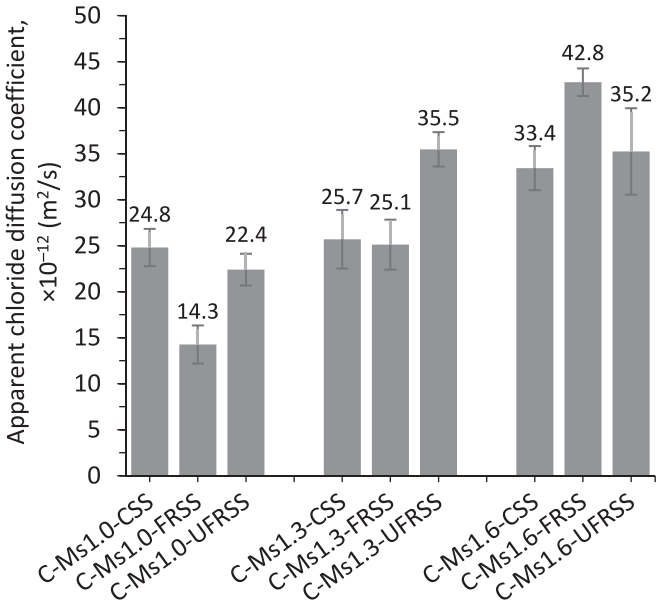


**Fig. 19.** Apparent chloride diffusion coefficients calculated from the chloride profile using the non-linear regression analysis.

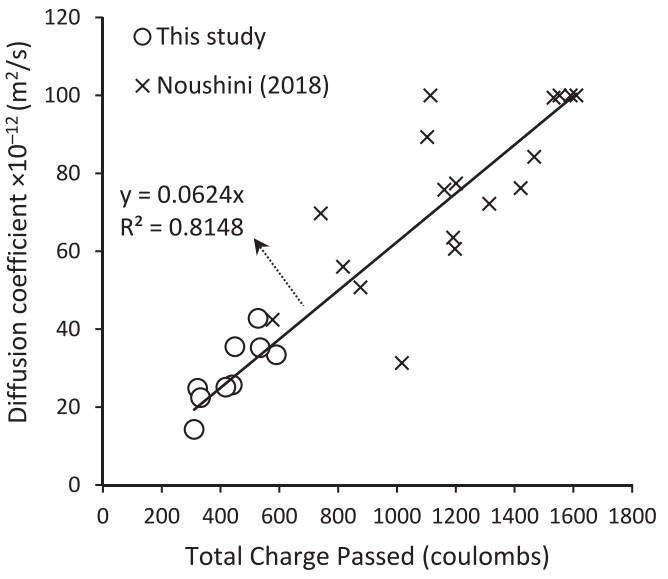


**Fig. 20.** Correlation between chloride diffusion coefficient and total charge passed at 10 V from this study and Noushini [72].

## 4. Conclusions

This paper provided a detailed investigation on the synthesis of rice husk ash (RHA)-derived sodium silicate (SSs) activators and the transport properties, such as water absorption and chloride penetration, of AAM concrete using RHA SSs. First, the effect of the extraction process on the oligomerisation of silicate species derived from RHA was thoroughly investigated. Mixtures of NaOH solution and RHA powder were heated and stirred at different durations and temperatures to facilitate the dissolution of silica from RHA into the NaOH solution. The availability and structure of silicate species were analysed using filtration, ICP-OES, ATR-FTIR, $^{29}$Si NMR, and viscosity tests.

In addition, the extracted sodium silicates were used in the preparation of AAM concrete to investigate compressive strength, water absorption, and chloride diffusion resistance. The following conclusions can be drawn:

- The extraction parameters, especially the mixing temperature, play an influential role in maximising the availability of silicates in the extracted solution. Low processing temperatures (< 80 °C) result in a lack of silicate availability in the RHA SS. On the other hand, the mixing duration had a minimal impact on the dissolution efficiency since marginal effects were observed when the mixing duration was increased from 1 h to 5 h. Therefore, in this study, the yield of silica was optimised using one hour of mixing at 80 °C.
- While monomer, dimer, trimer, and tetramer silicate species were highly available in all solutions, higher mixing duration, temperature, and RHA/NaOH ratio affects oligomerisation of silicates. The increased concentration of silicates resulted in an increase in the Newtonian viscosity of the solution.
- In AAM concrete, an increase of about 14 % in the water absorption by immersion was observed by increasing the silica modulus from 1.0 to 1.6. The use of unfiltered RHA SS resulted in an increase of about 9 % in the water absorption, which is in a lower magnitude compared to that caused by the increase in silica modulus.

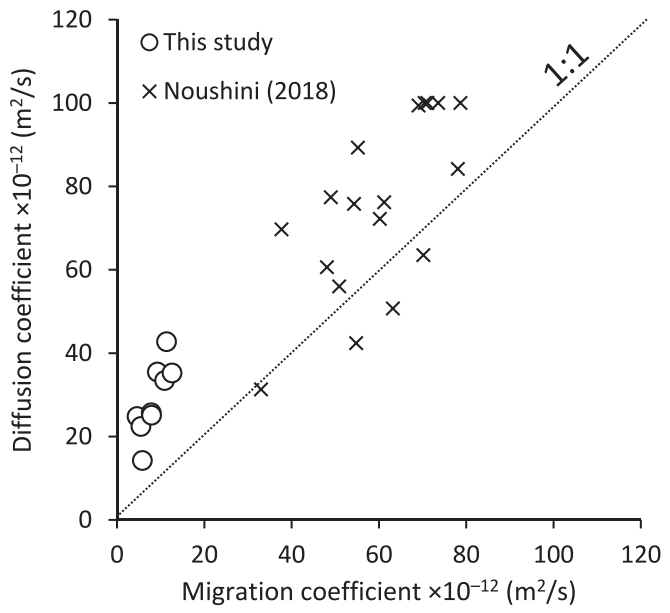


**Fig. 21.** Correlation between chloride diffusion and migration coefficients from this study and Noushini [72].

- The chloride transport results of concrete activated with commercial and RHA SSs revealed the insignificant effect of the type of SS compared to the effect of the silica modulus value.
- The use of NSSM test to characterise the ingress of chloride may lead to an underestimation of the extent of chloride resistance compared to the chloride diffusion test due to the effect of the pore solution pH of AAM concrete on the chloride concentration at the colour change boundary.
- The modified RCPT method (lowering the applied voltage to 10 *V*) seems to be a valid approach for AAM systems.

It should be highlighted that, although the dissolution parameters of the hydrothermal process affected the content and structure of silicates in the RHA SSs, their performance in AAM concrete seems to be acceptable. However, a careful design of the mix components is essential, especially by considering the actual concentration of soluble silicates in the activator. The outcomes of this study promote the use of waste-derived activators technology for sustainable production of AAM concrete with comparable mechanical and transport properties to those of AAM concrete using commercial activators.

## CRediT authorship contribution statement

**Mohammed Fouad Alnahhal:** Writing – original draft, Visualization, Validation, Methodology, Investigation, Formal analysis, Data curation, Conceptualization. **Abdelrahman Hamdan:** Writing – review & editing, Investigation, Formal analysis, Data curation. **Ailar Hajimohammadi:** Writing – review & editing, Validation, Supervision, Methodology, Conceptualization. **Arnaud Castel:** Writing – review & editing, Methodology, Formal analysis. **Taehwan Kim:** Writing – review & editing, Validation, Supervision, Resources, Project administration, Methodology, Funding acquisition, Formal analysis, Conceptualization.

## Declaration of competing interest

The authors declare that they have no known competing financial interests or personal relationships that could have appeared to influence the work reported in this paper.

## Data availability

Data will be made available on request.

## Acknowledgments

This work was supported by the Australian Government Research Training Program Scholarship. The authors also acknowledge the support provided by the academic start-up fund from the faculty of engineering at UNSW Sydney.

## Appendix A. Supplementary data

Supplementary data to this article can be found online at https://doi.org/10.1016/j.cemconres.2024.107461.

## References

[1] USGS, Cement - Mineral Commodity Summaries, Cement Statistics and Information - Annual Publications, U.S. Geological Survey, 2022.
[2] K.L. Scrivener, V.M. John, E.M. Gartner, Eco-efficient cements: potential economically viable solutions for a low-CO2 cement-based materials industry, Cem. Concr. Res. 114 (2018) 2–26.
[3] L. Coppola, T. Bellezze, A. Belli, M.C. Bignozzi, F. Bolzoni, A. Brenna, M. Cabrini, S. Candamano, M. Cappai, D. Caputo, Binders alternative to Portland cement and waste management for sustainable construction—part 1, J. Appl. Biomater. Funct. Mater. 16 (2018) 186–202.
[4] C. Shi, A.F. Jiménez, A. Palomo, New cements for the 21st century: the pursuit of an alternative to Portland cement, Cem. Concr. Res. 41 (2011) 750–763.
[5] M.C. Juenger, R. Snellings, S.A. Bernal, Supplementary cementitious materials: new sources, characterization, and performance insights, Cem. Concr. Res. 122 (2019) 257–273.
[6] G. Habert, J.D.E. De Lacaillerie, N. Roussel, An environmental evaluation of geopolymer based concrete production: reviewing current research trends, J. Clean. Prod. 19 (2011) 1229–1238.
[7] A. Heath, K. Paine, M. McManus, Minimising the global warming potential of clay based geopolymers, J. Clean. Prod. 78 (2014) 75–83.
[8] M.F. Alnahhal, T. Kim, A. Hajimohammadi, Waste-derived activators for alkali-activated materials: a review, Cem. Concr. Compos. 103980 (2021).
[9] M. Torres-Carrasco, M.T. Tognonvi, A. Tagnit-Hamou, F. Puertas, Durability of alkali-activated slag concretes prepared using waste glass as alternative activator, ACI Mater. J. 112 (2015) 791.
[10] P. Pavithra, M.S. Reddy, P. Dinakar, B.H. Rao, B. Satpathy, A. Mohanty, A mix design procedure for geopolymer concrete with fly ash, J. Clean. Prod. 133 (2016) 117–125.
[11] A. Rafeet, R. Vinai, M. Soutsos, W. Sha, Guidelines for mix proportioning of fly ash/GGBS based alkali activated concretes, Constr. Build. Mater. 147 (2017) 130–142.
[12] L.K. Turner, F.G. Collins, Carbon dioxide equivalent (CO2-e) emissions: a comparison between geopolymer and OPC cement concrete, Constr. Build. Mater. 43 (2013) 125–130.
[13] R. Bajpai, K. Choudhary, A. Srivastava, K.S. Sangwan, M. Singh, Environmental impact assessment of fly ash and silica fume based geopolymer concrete, J. Clean. Prod. 254 (2020) 120147.
[14] K.T. Tong, R. Vinai, M.N. Soutsos, Use of Vietnamese rice husk ash for the production of sodium silicate as the activator for alkali-activated binders, J. Clean. Prod. 201 (2018) 272–286.
[15] M.F. Alnahhal, A. Hamdan, A. Hajimohammadi, T. Kim, Effect of rice husk ash-derived activator on the structural build-up of alkali activated materials, Cem. Concr. Res. 150 (2021) 106590.
[16] R. Vinai, M. Soutsos, Production of sodium silicate powder from waste glass cullet for alkali activation of alternative binders, Cem. Concr. Res. 116 (2019) 45–56.
[17] X. Dai, S. Aydın, M.Y. Yardımcı, K. Lesage, G. De Schutter, Rheology and microstructure of alkali-activated slag cements produced with silica fume activator, Cem. Concr. Compos. 125 (2022) 104303.
[18] Q. Alam, Y. Hendrix, L. Thijs, A. Lazaro, K. Schollbach, H. Brouwers, Novel low temperature synthesis of sodium silicate and ordered mesoporous silica from incineration bottom ash, J. Clean. Prod. 211 (2019) 874–883.
[19] A. Passuello, E.D. Rodriguez, E. Hirt, M. Longhi, S.A. Bernal, J.L. Provis, A. P. Kirchheim, Evaluation of the potential improvement in the environmental footprint of geopolymers using waste-derived activators, J. Clean. Prod. 166 (2017) 680–689.
[20] N. Bouzón, J. Payá, M. Borrachero, L. Soriano, M.M. Tashima, J. Monzó, Refluxed rice husk ash/NaOH suspension for preparing alkali activated binders, Mater. Lett. 115 (2014) 72–74.
[21] S.A. Bernal, E.D. Rodríguez, R.M. de Gutiérrez, J.L. Provis, S. Delvasto, Activation of metakaolin/slag blends using alkaline solutions based on chemically modified silica fume and rice husk ash, Waste Biomass Valoriz. 3 (2012) 99–108.
[22] J.L. Bass, G.L. Turner, Anion distributions in sodium silicate solutions. Characterization by 29Si NMR and infrared spectroscopies, and vapor phase osmometry, J. Phys. Chem. B 101 (1997) 10638–10644.

[23] H. Cho, A.R. Felmy, R. Craciun, J.P. Keenum, N. Shah, D.A. Dixon, Solution state structure determination of silicate oligomers by 29Si NMR spectroscopy and molecular modeling, J. Am. Chem. Soc. 128 (2006) 2324–2335.
[24] S. Aydın, B. Baradan, Mechanical and microstructural properties of heat cured alkali-activated slag mortars, Mater. Des. 35 (2012) 374–383.
[25] J. Mejía, R.M. de Gutiérrez, F. Puertas, Rice husk ash as a source of silica in alkali-activated fly ash and granulated blast furnace slag systems, Mater. Constr. 63 (2013) 361–375.
[26] J.M. Mejía, R.M. De Gutiérrez, C. Montes, Rice husk ash and spent diatomaceous earth as a source of silica to fabricate a geopolymeric binary binder, J. Clean. Prod. 118 (2016) 133–139.
[27] M.F. Alnahhal, U.J. Alengaram, M.Z. Jumaat, B. Alsubari, M.A. Alqedra, K.H. Mo, Effect of aggressive chemicals on durability and microstructure properties of concrete containing crushed new concrete aggregate and non-traditional supplementary cementitious materials, Constr. Build. Mater. 163 (2018) 482–495.
[28] F. Puertas, M. Torres-Carrasco, Use of glass waste as an activator in the preparation of alkali-activated slag. Mechanical strength and paste characterisation, Cem. Concr. Res. 57 (2014) 95–104.
[29] M. Samarakoon, P. Ranjith, W.H. Duan, V. De Silva, Properties of one-part fly ash/slag-based binders activated by thermally-treated waste glass/NaOH blends: a comparative study, Cem. Concr. Compos. 112 (2020) 103679.
[30] ASTM C1202, Standard Test Method for Electrical Indication of Concrete's Ability to Resist Chloride Ion Penetration, ASTM International, West Conshohocken, PA, 2012.
[31] NT Build 492, Concrete, Mortar and Cement-Based Repair Materials: Chloride Migration Coefficient from Non-steady-State Migration Experiments, Nordtest, Espoo, Finland, 1999.
[32] ASTM C1556, Standard Test Method for Determining the Apparent Chloride Diffusion Coefficient of Cementitious Mixtures by Bulk Diffusion, ASTM International, West Conshohocken, PA, 2016.
[33] ASTM C618, Standard Specification for Coal Fly Ash and Raw or Calcined Natural Pozzolan for Use in Concrete, ASTM International, West Conshohocken, PA, 2012.
[34] M. Torres-Carrasco, J.G. Palomo, F.P. Maroto, Sodium silicate solutions from dissolution of glasswastes. Statistical analysis, Mater. Constr. (2014) 3.
[35] H.K. Tchakouté, C.H. Rüscher, S. Kong, N. Ranjbar, Synthesis of sodium waterglass from white rice husk ash as an activator to produce metakaolin-based geopolymer cements, J. Build. Eng. 6 (2016) 252–261.
[36] B. Koohestani, P. Mokhtari, E. Yilmaz, F. Mahdipour, A.K. Darban, Geopolymerization mechanism of binder-free mine tailings by sodium silicate, Constr. Build. Mater. 268 (2021) 121217.
[37] ASTM C192, Standard Practice for Making and Curing Concrete Test Specimens in the Laboratory, ASTM International, West Conshohocken, PA, 2015.
[38] ASTM C39, Standard Test Method for Compressive Strength of Cylindrical Concrete Specimens, ASTM International, West Conshohocken, PA, 2015.
[39] ASTM C642, Standard Test Method for Density, Absorption, and Voids in Hardened Concrete, ASTM International, West Conshohocken, PA, 2013.
[40] ASTM C1585, Measurement of Rate of Absorption of Water by Hydraulic-Cement Concretes, ASTM International, West Conshohocken, PA, 2013.
[41] X.-M. Cui, G.-J. Zheng, Y.-C. Han, F. Su, J. Zhou, A study on electrical conductivity of chemosynthetic Al2O3–2SiO2 geoplymer materials, J. Power Sources 184 (2008) 652–656.
[42] S. Hanjitsuwan, S. Hunpratub, P. Thongbai, S. Maensiri, V. Sata, P. Chindaprasirt, Effects of NaOH concentrations on physical and electrical properties of high calcium fly ash geopolymer paste, Cem. Concr. Compos. 45 (2014) 9–14.
[43] A. Noushini, A. Castel, Performance-based criteria to assess the suitability of geopolymer concrete in marine environments using modified ASTM C1202 and ASTM C1556 methods, Mater. Struct. 51 (2018) 1–16.
[44] ASTM C1152, Standard Test Method for Acid-Soluble Chloride in Mortar and Concrete, ASTM International, West Conshohocken, PA, 2020.
[45] H. Maraghechi, F. Rajabipour, C.G. Pantano, W.D. Burgos, Effect of calcium on dissolution and precipitation reactions of amorphous silica at high alkalinity, Cem. Concr. Res. 87 (2016) 1–13.
[46] T. Kim, J. Olek, Chemical sequence and kinetics of alkali–silica reaction part II. A thermodynamic model, J. Am. Ceram. Soc. 97 (2014) 2204–2212.
[47] P.V. Brady, J.V. Walther, Controls on silicate dissolution rates in neutral and basic pH solutions at 25 C, Geochim. Cosmochim. Acta 53 (1989) 2823–2830.
[48] P.M. Dove, D.A. Crerar, Kinetics of quartz dissolution in electrolyte solutions using a hydrothermal mixed flow reactor, Geochim. Cosmochim. Acta 54 (1990) 955–969.
[49] T.T. Trinh, A.P. Jansen, R.A. van Santen, Mechanism of oligomerization reactions of silica, J. Phys. Chem. B 110 (2006) 23099–23106.
[50] X. Yang, P. Roonasi, A. Holmgren, A study of sodium silicate in aqueous solution and sorbed by synthetic magnetite using in situ ATR-FTIR spectroscopy, J. Colloid Interface Sci. 328 (2008) 41–47.
[51] D. Dimas, I. Giannopoulou, D. Panias, Polymerization in sodium silicate solutions: a fundamental process in geopolymerization technology, J. Mater. Sci. 44 (2009) 3719–3730.
[52] D.-W. Zhang, D.-m. Wang, Z. Liu, F.-z. Xie, Rheology, agglomerate structure, and particle shape of fresh geopolymer pastes with different NaOH activators content, Constr. Build. Mater., 187 (2018) 674–680.
[53] H. Jansson, D. Bernin, K. Ramser, Silicate species of water glass and insights for alkali-activated green cement, AIP Adv. 5 (2015) 067167.
[54] A. Borba, J. Vareda, L. Durães, A. Portugal, P. Simões, Spectroscopic characterization of silica aerogels prepared using several precursors–effect on the formation of molecular clusters, New J. Chem. 41 (2017) 6742–6759.
[55] R.K. Harris, E.K. Bahlmann, K. Metcalfe, E.G. Smith, Quantitative silicon-29 NMR investigations of highly concentrated high-ratio sodium silicate solutions, Magn. Reson. Chem. 31 (1993) 743–747.
[56] L. Engelhardt, D. Zeigan, H. Jancke, W. Wieker, D. Hoebbel, 29Si-NMR-Spektroskopie an Silicatlösungen. II. Zur Abhängigkeit der Struktur der Silicatanionen in wäßrigen Natriumsilicatlösungen vom Na: Si-Verhältnis, Z. Anorg. Allg. Chem. 418 (1975) 17–28.
[57] N.H. Ray, R.J. Plaisted, The constitution of aqueous silicate solutions, J. Chem. Soc. Dalton Trans. (1983) 475–481.
[58] I.L. Svensson, S. Sjöberg, L.-O. Öhman, Polysilicate equilibria in concentrated sodium silicate solutions, Journal of the Chemical Society, Faraday Transactions 1: Physical Chemistry in Condensed Phases, 82 (1986) 3635–3646.
[59] L. Vidal, E. Joussein, M. Colas, J. Cornette, J. Sanz, I. Sobrados, J. Gelet, J. Absi, S. Rossignol, Controlling the reactivity of silicate solutions: a FTIR, Raman and NMR study, Colloids Surf. A Physicochem. Eng. Asp. 503 (2016) 101–109.
[60] J.L. Bass, G.L. Turner, M.D. Morris, Vibrational and 29Si NMR Spectroscopies of Soluble Silicate Oligomers, Macromolecular Symposia, Wiley Online Library, 1999, pp. 263–270.
[61] S.D. Kinrade, T.W. Swaddle, Silicon-29 NMR studies of aqueous silicate solutions. 1. Chemical shifts and equilibria, Inorg. Chem. 27 (1988) 4253–4259.
[62] A. Noushini, A. Castel, The effect of heat-curing on transport properties of low-calcium fly ash-based geopolymer concrete, Constr. Build. Mater. 112 (2016) 464–477.
[63] S. Aydın, B. Baradan, Effect of activator type and content on properties of alkali-activated slag mortars, Compos. Part B Eng. 57 (2014) 166–172.
[64] J.L. Provis, R.J. Myers, C.E. White, V. Rose, J.S. van Deventer, X-ray microtomography shows pore structure and tortuosity in alkali-activated binders, Cem. Concr. Res. 42 (2012) 855–864.
[65] M. Babaee, A. Castel, Chloride diffusivity, chloride threshold, and corrosion initiation in reinforced alkali-activated mortars: role of calcium, alkali, and silicate content, Cem. Concr. Res. 111 (2018) 56–71.
[66] T.-H. Ha, S. Muralidharan, J.-H. Bae, Y.-C. Ha, H.-G. Lee, K.W. Park, D.-K. Kim, Effect of unburnt carbon on the corrosion performance of fly ash cement mortar, Constr. Build. Mater. 19 (2005) 509–515.
[67] N.-H. Kang, C.-M. Chon, H.-T. Jou, S. Lee, Effect of particle size and unburned carbon content of fly ash from Hadong power plant on compressive strength of geopolymers, Korean, J. Mater. Res. 23 (2013) 510–516.
[68] A.M. Zeyad, M.M. Johari, B.A. Tayeh, M.O. Yusuf, Efficiency of treated and untreated palm oil fuel ash as a supplementary binder on engineering and fluid transport properties of high-strength concrete, Constr. Build. Mater. 125 (2016) 1066–1079.
[69] S. Muthukrishnan, S. Gupta, H.W. Kua, Application of rice husk biochar and thermally treated low silica rice husk ash to improve physical properties of cement mortar, Theor. Appl. Fract. Mech. 104 (2019) 102376.
[70] P.S. Deb, P.K. Sarker, S. Barbhuiya, Sorptivity and acid resistance of ambient-cured geopolymer mortars containing nano-silica, Cem. Concr. Compos. 72 (2016) 235–245.
[71] P.H. Borges, N. Banthia, H.A. Alcamand, W.L. Vasconcelos, E.H. Nunes, Performance of blended metakaolin/blastfurnace slag alkali-activated mortars, Cem. Concr. Compos. 71 (2016) 42–52.
[72] A. Noushini, Durability of Geopolymer Concrete in Marine Environment, School of Civil and Environmental Engineering, Faculty of Engineering, UNSW, Sydney, Australia, 2018.
[73] M. Soutsos, A.P. Boyle, R. Vinai, A. Hadjierakleous, S.J. Barnett, Factors influencing the compressive strength of fly ash based geopolymers, Constr. Build. Mater. 110 (2016) 355–368.
[74] A. Noushini, Q.D. Nguyen, A. Castel, Assessing alkali-activated concrete performance in chloride environments using NT build 492, Mater. Struct. 54 (2021) 1–15.
[75] N. Lee, H.-K. Lee, Influence of the slag content on the chloride and sulfuric acid resistances of alkali-activated fly ash/slag paste, Cem. Concr. Compos. 72 (2016) 168–179.
[76] Y. Ma, G. Ye, The shrinkage of alkali activated fly ash, Cem. Concr. Res. 68 (2015) 75–82.
[77] M. Mastali, P. Kinnunen, A. Dalvand, R.M. Firouz, M. Illikainen, Drying shrinkage in alkali-activated binders–a critical review, Constr. Build. Mater. 190 (2018) 533–550.